Marine Geology 402 (2018) 264–278

Contents lists available at ScienceDirect

Marine Geology

journal homepage: www.elsevier.com/locate/margo

Sediment properties in submarine mass-transport deposits using seismic and rock-physics off NW Barents Sea

Gianni Madrussani[a,*], Giuliana Rossi[a], Michele Rebesco[a], Stefano Picotti[a], Roger Urgeles[b], Jaume Llopart[b]

[a] Istituto Nazionale di Oceanografia e di Geofisica Sperimentale-OGS, Borgo Grotta Gigante 42/c, Sgonico, Trieste, Italy
[b] Institut de Ciències del Mar (CSIC), Passeig Marítim de la Barceloneta, 37-49, Barcelona, Spain

ARTICLE INFO

Keywords:
Mass-transport deposits
NW Barents Sea margin
Rock physics
Travel-time and attenuation tomography

ABSTRACT

Submarine mass movements may have profound effects on the morphology and stratigraphic architecture of continental margins. Furthermore, they can represent a threat to human life and infrastructures, and also have implications for hydrocarbon exploration/production. In polar regions, they are one of the predominant sedimentary processes on the continental slope. Exploration seismology has been widely employed to study mass-transport deposits (landslides, glacigenic debris flows, mass flows, etc.), which are usually characterized by chaotic reflections. In this study, we analyse a seismic profile acquired in the southern part of the Storfjorden trough mouth fan (NW Barents Sea margin), showing the presence of two submarine mass-transport deposits (MTDs). A giant MTD (PLS-1) is located on the lower continental slope at 2.6–3 km depth, while a more recent MTD (PLS-2) occurs at 1.9–2.4 km depth. Velocity and attenuation seismic tomography, seismic attributes analyses and rock-physics models reveal distinct petrophysical properties for PLS-1 and PLS-2. Despite the known influence of burial depth(s), fluid flow content, and compaction on the internal character of MTDs, the two deposits studied here, in fact, show distinct petrophysical characteristics that reflect lithological variations - more than to any other control. These results suggest different source areas for the two MTDs. The inferred coarser sediment in PLS-1 indicates provenance from areas with abundant glacigenic debris flows, (such as the Bjørnøya Trough-Mouth Fan). Conversely, the finer, relatively fluid-rich sediments of PLS-2 that underwent little translation could have an origin in the area between trough-mouth fans. Here, slow-moving ice resulted in a relatively scarce release of subglacial debris at the shelf edge and the continental slope was subject to enhanced erosion and degradation with a comparatively higher production of relatively fine-grained turbidite flows.

1. Introduction

Mass movements occur on all continental slopes and represent a major mechanism controlling stratigraphic architecture and slope morphology (Yamada et al., 2012). Mass movements allow a redistribution of sediments, which are transported downslope from the shelf and upper slope towards the deeper part of the basin (Dondurur and Çifçi, 2007; Rebesco et al., 2009; Ogata et al., 2014). Moreover, submarine mass movements represent a critical offshore geohazard that threatens human life and engineering structures and have significant implications for a sustainable development of the marine environment (Chiocci et al., 2011; Yamada et al., 2012). Some of the largest mass-transport deposits (MTDs) on Earth occur on high-latitude continental margins (Bugge et al., 1987; Laberg et al., 2002; Imbo et al., 2003; Diviacco et al., 2006; Vanneste et al., 2006; Hjelstuen et al., 2007; Donda et al., 2008; Rebesco and Camerlenghi, 2008; Volpi et al., 2011; Safronova et al., 2012; Mosher et al., 2012, 2017; Omosanya et al., 2016), where they also constitute a significant proportion of the sedimentary sequence. The onset mechanism for these slope failures includes a mix of triggering and preconditioning factors such as earthquakes, rapid sediment loading, excess pore pressures, deposition of weak sedimentary layers, and gas hydrate dissociation (Sultan et al., 2004; Solheim et al., 2005; Gales et al., 2014; Llopart et al., 2015).

A high number of MTDs are present on the continental slope of the Storfjorden and Kveithola Trough Mouth Fans (TMFs) on the NW Barents Sea margin (Dowdeswell and Kenyon, 1995; Vorren et al., 1998; Rebesco et al., 2012; Lucchi et al., 2012; Llopart et al., 2014). They are associated with major glacially-sourced depocenters juxtaposed with sediment-starved and degraded areas developed since about 1 Ma ago (Rebesco et al., 2012) when the Barents Sea/Svalbard Ice

* Corresponding author.
E-mail address: gmadrussani@inogs.it (G. Madrussani).

https://doi.org/10.1016/j.margeo.2017.11.013
Received 22 December 2016; Received in revised form 10 November 2017; Accepted 23 November 2017
Available online 27 November 2017

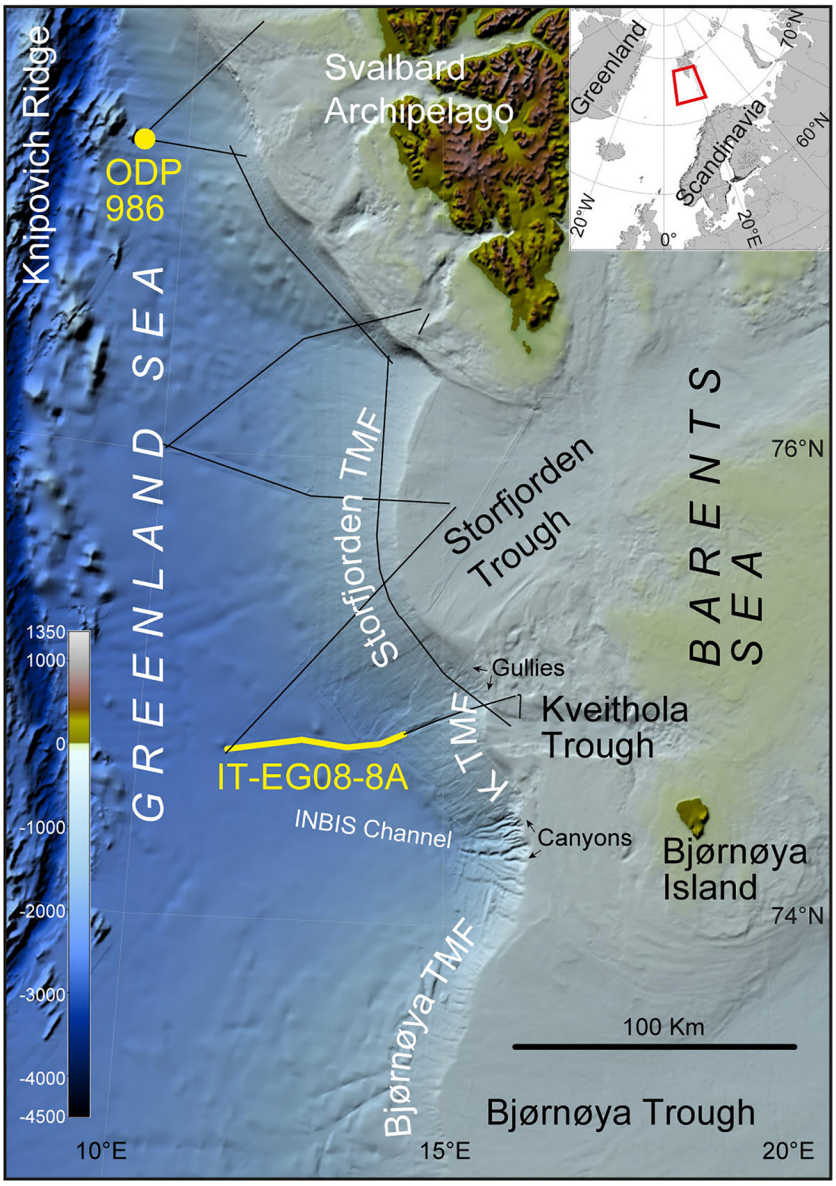

Fig. 1. Bathymetric map of the study area from IBCAO (Jakobsson et al., 2012), with indicated the main geographical features, and the location of the MCS profiles acquired during the EGLACOM survey. Profile IT-EG08B is highlighted in yellow. ODP Site 986 is also shown. K TMF = Kveithola Through Mouth Fan. Arrows indicate the presence of canyons and gullies. Location of the study area within a more general geographic context is displayed in the top-right inset. (For interpretation of the references to color in this figure legend, the reader is referred to the web version of this article.)

Sheet reached the shelf edge (Rebesco et al., 2014). We analyse two large MTDs, possibly originated from two different parts of the margin and previously identified by Rebesco et al. (2012) as PLS-1 and PLS-2 on a limited grid of 2D seismic data. In fact, MTDs are best studied when industrial three-dimensional seismic volumes and borehole data are available, allowing detailed geophysical investigations and sedimentological and geotechnical analyses (e.g., Alves et al., 2014; Baeten et al., 2014). However, like in the case studied in this paper, researchers have often to rely on sparse and incomplete datasets.

The purpose of this study is to present a novel procedure, helpful when forced to contend with the scarcity of seismic profiles and the absence of direct measurements from nearby boreholes. The process involves applying different analytical techniques (velocity and attenuation tomographic inversion, attribute analysis and advanced processing) to a single multichannel seismic reflection profile, and rock-physics modeling to a far-off borehole. The case study of a seismic profile recorded off the Kveithola TMF and the remote ODP Site 986 demonstrates the possibility of inferring the geometry, petrophysical properties, and origin of MTDs and reconstructs their depositional processes.

2. Geological setting

Along glacially influenced margins, one of the primary mechanisms of sediment delivery is at the mouth of glacially-carved troughs to form sedimentary fans, known as trough mouth fans (Vorren and Laberg, 1997; Vorren et al., 1998). These TMFs are mainly composed of stacked glacigenic debris flow deposits delivered beyond the shelf-break by fast-flowing ice streams (Vorren and Laberg, 1997; Dowdeswell et al., 1998; Ó Cofaigh et al., 2003). Glacial debris, delivered during glacial maxima, (when ice sheets extended to the shelf edge), alternates with plumites, hemipelagic and contour-current deposits that accumulated during interglacial and deglacial periods (Lucchi et al., 2013; Rebesco et al., 2016). The Storfjorden and Kveithola TMFs are two such glacial-marine sedimentary systems located in the NW Barents Sea (Fig. 1). They were influenced by the action of fast-moving ice streams during the late Cenozoic (Laberg and Vorren, 1996a,b; Rebesco et al., 2011; Hanebuth et al., 2014).

Channels originated by canyon and gully systems are unusual along the Norwegian margin (Ó Cofaigh et al., 2006). They developed between ice streams, where the ice was moving slower, and the continental slope was relatively starved and degraded (Vorren et al. 1998;

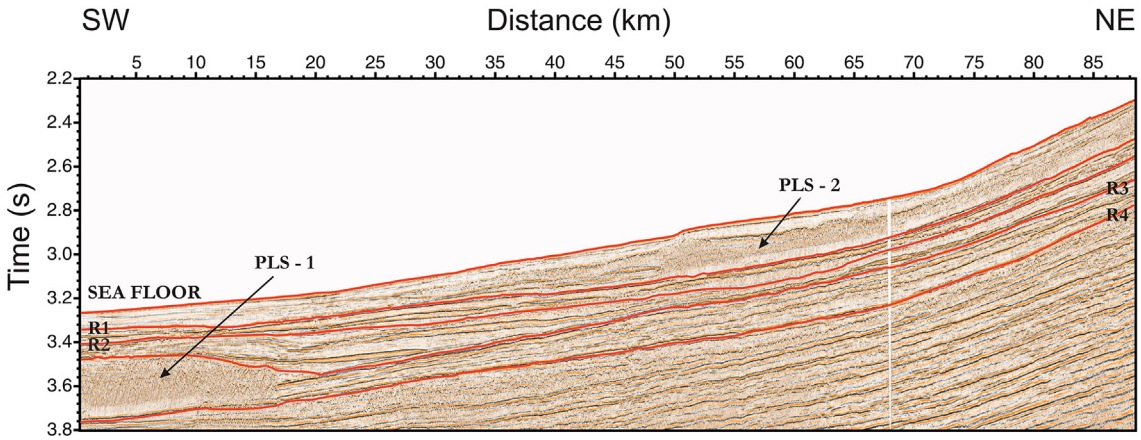

Fig. 2. Profile IT-EG08B (see location in Fig. 1). Stacked section showing the picked horizons (R1–R4 and sea-floor). The two MTDs analysed (PLS-1 and PLS-2) are indicated by arrows. X-axis: distance from the start of the line (SW) in km. Y-axis: TWT (s). The age of the picked reflectors is: 0.2 Ma (R1), 0.5 Ma (R2), 0.75 Ma (R3), and 1.1 Ma (R4).

Dowdeswell and Elverhøi, 2002; Taylor et al., 2002). Canyons, eroded by glacigenic debris flows and turbidity currents, are preserved due to the relatively low sedimentation rates compared to the adjacent TMFs (Taylor et al., 2000). Along this margin, in fact, the channels are limited to the INBIS Channel, which lies south of Kveithola (Fig. 1). This arrangement seems somehow different from submarine fans seaward of mid-latitude glacial ice streams (e.g., Laurentian Fan, Piper et al., 2016) where meltwater discharge appears to play a more significant role, reflected in the growth of well-developed channel-levee systems. Several MTDs have been identified on the Storfjorden-Kveithola margin (Hjelstuen et al., 1996; Sauli et al., 2010; Pedrosa et al., 2011; Rebesco et al., 2012; Lucchi et al., 2012; Llopart et al., 2015). The Kveithola MTD complex (one of the greatest MTDs of the Norwegian/Barents/Svalbard margin) was first recognized from GLORIA long-range side-scan sonar and 3.5 kHz data (Dowdeswell and Kenyon, 1995; Vorren et al., 1998; Taylor et al., 2002). The two MTDs PLS-1 and PLS-2 (Rebesco et al., 2012) belonging to the Kveithola MTD complex are located in the embayment formed in between the Storfjorden and Bjørnøya TMFs (Fig. 1). Within this embayment, the Kveithola TMF represents a minor sedimentary body between the southernmost part of the Storfjorden TMF and the gully system that converges towards the INBIS Channel. The headwall scar of PLS-2 was identified by Rebesco et al. (2012) between the Storfjorden and Kveithola TMFs. Conversely, MTD PLS-1 was inferred by Rebesco et al. (2012) to have originated from the southern part of the Storfjorden TMF or the northern part of the Bjørnøya TMFs, as PLS-1 lies just in between the two fans (Fig. 1). If the MTDs PLS-1 and PLS-2 originated from different parts of the margin, different mechanical behaviours might also be expected for the two MTDs.

Along the western Barents Sea and Svalbard margin, seven regional reflections (R1–R7) are recognized between the oceanic basement and the sea-floor (Faleide et al., 1996). These reflectors have been related to the main phases of glacial erosion and sedimentation, starting 2.3 Ma ago (Faleide et al., 1996; Fiedler and Faleide, 1996; Hjelstuen et al., 1996; Butt et al., 2000). In particular, Forsberg et al. (1999) concluded that the sequences delineated by horizons R1–R4 are composed of turbidites and debris flows interbedded with hemipelagic sediments. According to Rebesco et al. (2014), the age of these horizons is 0.2 Ma, 0.4 Ma, 0.75 Ma, 1.1 Ma, respectively. The basal detachment surface of MTD PLS-2 corresponds to horizon R1, whereas detachment of PLS-1 occurs between reflections R3 and R4 (see Fig. 2).

3. Data and methods

The data in this paper were acquired on the southern margin of Svalbard, in summer 2008, during a research cruise carried out in the frame of the Italian EGLACOM project (International Polar Year - IPY) onboard R/V OGS-Explora (Fig. 1). Data acquisition included multi-channel reflection seismic, swath bathymetry and sub-bottom profiler data.

The acquisition of the eleven multi-channel seismic profiles (for a total length of 1071 km) used a 96-channel digital streamer equipped with hydrophones spaced 12.5 m apart. Acoustic wave energy was generated using a 2.62 l array of sleeve guns. The sampling interval was 1 ms, while the shot interval was 25 m, resulting in a maximum of 24-fold coverage.

The acquisition pattern used in the seismic survey aimed at covering most of the continental margin between southern Svalbard and Bjørnøya so that the profiles intersect only minimally. No well-logs are available in the study area, the nearest site being ODP Site 986 about 200 km to the north. DSDP Site 344 was not considered in this study because it is condensed (< 400 m from sea-floor to basement, corresponding to a mean sedimentation rate of 7.6 cm/kyr) and it has lower core recovery (41%) than ODP site 986. Moreover, it is not directly correlatable to our seismic grid, and the few analyses on the core samples are mainly focused on geochemistry and biostratigraphy.

Seismic data processing aimed to produce stacked sections included a t-squared scaling factor, multi-channel shot spiking deconvolution, time-varying band-pass filtering trace equalisation and velocity analysis (see Rebesco et al., 2012). The present study focuses on seismic profile IT-EG08B, which intersects the two MTDs (Fig. 2). Further to the stacked section, we present new images, resulting from the application of other analytical techniques to the prestack raw data, to which no processing that could affect amplitudes or frequency content was applied. These techniques include: traveltime and attenuation tomographic inversion to obtain reliable velocity and attenuation depth models, prestack Kirchoff depth migration, seismic attribute analysis, and rock-physics modeling to achieve the porosity field and clay content (Fig. 3) (for details see Supplements). We focused modeling and interpretation on the shallow sedimentary succession below the sea-floor (upper 600 ms TWT, corresponding to about 500 m below sea-floor), where horizons R1 to R4 are recognized.

3.1. Seismic properties analysis

Seismic velocity is one of the most important geophysical parameters, being influenced by the vertical and lateral variation of density and elastic parameters (bulk and shear moduli), which in turn are mainly related to porosity and grain density. We use the tomographic method described in the Supplements to resolve vertical as well as lateral velocity gradients, to reconstruct the geological structures, and, hence, an adequate elastic velocity model in depth. We picked five

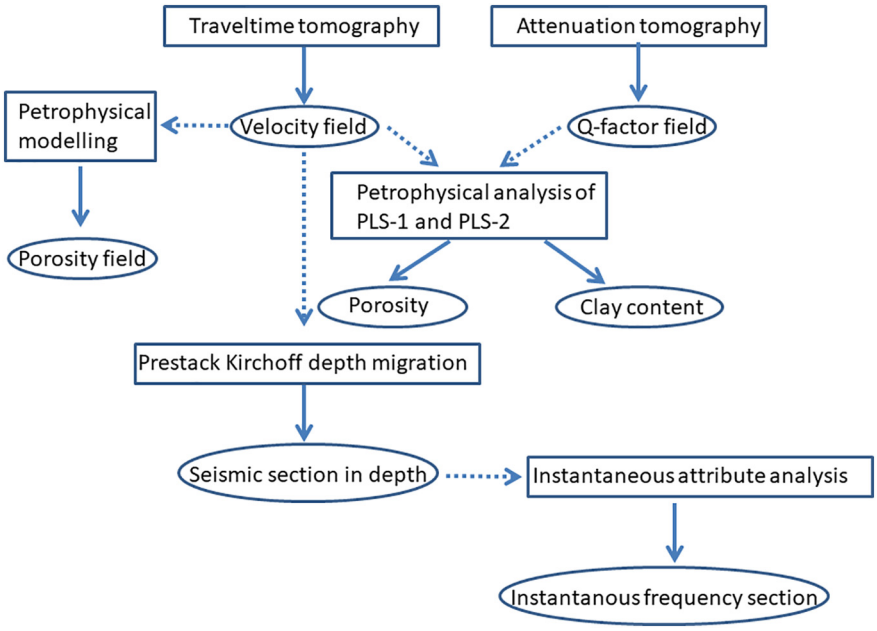

Fig. 3. Flow-chart of the analyses performed on the seismic data. Rectangles: methods; ellipses: outputs; solid line arrows: results; dotted arrows: input for the following step.

reflections (R1 to R4 plus the sea-floor) on the stacked section of profile IT-EG08B (Fig. 2). The obtained velocity field consists of four layers below the sea-floor, with a lateral resolution of 0.3 km. Further smoothed, it was used as input for a Kirchoff prestack depth migration to produce a depth-domain seismic image. Instantaneous attribute analysis (Taner et al., 1979; Matheney and Nowack, 1995) was performed on the migrated section, to retrieve information about reflection strength (instantaneous amplitude), energy absorption (instantaneous frequency) and the continuity of events along the margin and within the MTDs (instantaneous phase).

Permeability, porosity, saturation, and viscosity of the pore fluids influence the amplitude and frequency content of the seismic waves, causing their attenuation. The attenuation of P waves is usually quantified by the seismic quality factor (Q_p), which is proportional to the inverse of the loss of energy per wavelength (see Supplements). To obtain a Q_p field comparable with the velocity one, we use the attenuation tomography (Rossi et al., 2007, see Supplements for the details). We considered the same layers as for velocity, but a coarser grid (see Supplements), obtaining a Q_p field with a lateral resolution of 1 km.

3.2. Physical properties modeling: the porosity

To estimate the porosity distribution, we considered the methodology described in the Supplements and the mineral composition and logs at ODP Site 986 (Jansen et al., 1996; Forsberg et al., 1999) down to a depth of 180 m, the depth at which the R4 reflection is tied to the borehole. This borehole is the only drilling site crossed by our seismic grid and the one that best reproduces the mineralogical information for our investigated area. We verified that mineral composition remains almost constant with depth at the average wavelength scale of the seismic signal, which is about 50 m, and it is dominated by clay, quartz, and feldspar. A minor presence of other minerals does not affect the porosity computation significantly. The volume fraction range is 51–58% clay, 28–35% quartz and 3.6–7% for the feldspar. The physical properties of each mineral component are shown in Table 1.

We also used the available sonic-log records to calibrate the exponential dimensionless parameter A in the Krief relationship (see Supplements). The geothermal gradient at ODP Site 986 is 152 °C/km, whereas the water temperature at a depth of 2.4 km is − 1 °C (Jansen et al., 1996) and the average salinity is 30,000 ppm. Using the empirical relations suggested by Batzle and Wang (1992), it follows that the brine density and bulk modulus at the maximum depth of 180 m below the sea bottom, at ODP Site 986, are $\rho_b = 1026$ kg/m^3 and $K_b = 2.52$ GPa, which correspond to a temperature of about 26 °C.

Table 1
Typical values for grain bulk modulus (K), shear modulus (μ) and density (ρ) (Schön, 1996; Wang et al., 2001). Average volume fraction (β_i) of each component computed along the ODP site 986 down to 180 m depth.

Component	K_i (GPa)	μ_i (GPa)	ρ_i (kg/m^3)	β_i
Quartz	37.2	44.3	2650	33
Feldspar	37.5	15	2620	6
Clay	20.9	6.9	2580	56

The value of the geothermal gradient at the ODP Site 986 is abnormally high because it is located close to the Knipovich Ridge. The gradient is therefore not suitable for our study area. Vanneste et al. (2005) showed that moving away from the Molloy Transform, the geothermal gradient decreases by about 1 °C/km per horizontal km. At 50 km from the Molloy Transform, the geothermal gradient should, therefore, be ~63 °C/km (also confirmed by Dumke et al., 2016). Considering that our study area is located at a minimum distance of about 66 km from the Knipovich Ridge (which is the continuation of the Molloy Transform), it follows that an average value of 50 °C/km for the geothermal gradient is plausible.

3.3. Physical properties analysis of PLS-1 and PLS-2

To better analyse the petrophysical parameters of the two MTDs, we computed the average clay content and porosity of PLS-1 and PLS-2 by considering the frequency dependence of the attenuation and velocity dispersion due to the mesoscopic-loss effect (White, 1975; White et al., 1975; see Supplements). Böhm et al. (2015) were the first to use this approach to estimate clay-content and gas saturation in a synthetic geologic model from simulated seismograms, but to our knowledge, it has never been applied on real seismic data. In a recent work, Anwar et al. (2017) suggest a Bayesian inversion procedure to assess fluid and shale content in sand-shale media from synthetic amplitude versus offset data.

This analysis aims to simultaneously match the average tomographic P-wave velocity and quality factor for PLS-1 and PLS-2 (Böhm

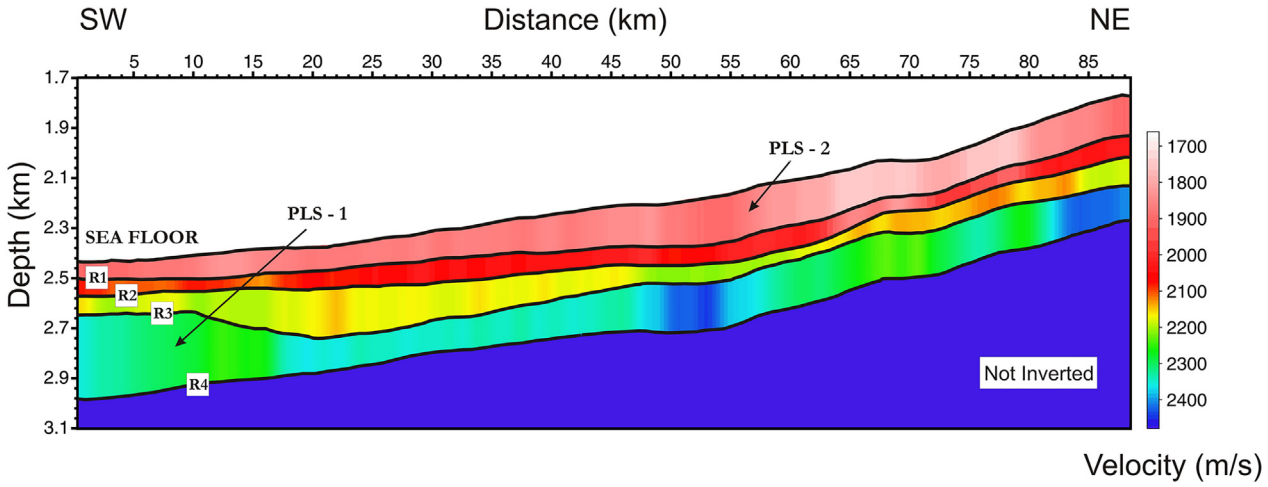

Fig. 4. Profile IT-EG08B. Tomographic velocity field, the layers are limited by the reflections shown in Fig. 2 (R1–R4 and sea-floor). X-axis: distance from the start of the line (SW) in km. Y-axis: depth (km).

et al., 2015), under the assumption that the medium is a fully brine-saturated shaly sandstone (case F4 described in Carcione and Picotti, 2006). Using the empirical relations of Batzle and Wang (1992) and an average oceanic crust geothermal gradient of 50 °C/km, we found that the average brine density, bulk modulus and viscosity for PLS-1 are ρ_b = 1030 kg/m^3, K_b = 2.49 GPa and η_b = 1.09 cp (corresponding to a temperature of about 19 °C), respectively. The values for PLS-2 are ρ_b = 1031 kg/m^3, K_b = 2.33 GPa and η_b = 1.43 cp (corresponding to a temperature of about 7 °C).

Thus, we consider two different frames, sandstone and shale (with proportions p1 and p2, see Supplements), whose grain properties are those of quartz and clay in Table 1, respectively. We also assume that the grain diameters are 80 μm for sandstone and 0.3 μm for clay, as in Carcione and Picotti (2006). We vary the porosity of sandstone (Φ_1) and clay (Φ_2), the shale proportion p_2, (hereafter referred to as clay content) and the parameter A for the exponent of the Krief relation until both the theoretical velocity and quality factor, computed using Eq. (1) of the Supplements, match the corresponding average tomographic values within the experimental errors. We vary the value A in a range from 1.5 to 3 for sandstone and from 3 to 6 for clay (the pore shape is more crack-like for clay than for sandstone). The maximum size of the heterogeneities (sandstone and clay patches) is assumed to be 2 m for glacigenic sediments, which is large enough to cover a sufficient range of sizes. The minimum size depends only on the incremental step, a percentage clay content of 0.5%, which implies a minimum size of 1 mm. This value is chosen to achieve the solution in a reasonable computational time.

Finally, we compute the average clay content and porosity of the two MTDs by averaging all values retrieved by the iterative procedure.

4. Results

4.1. Seismic stratigraphy and seismic facies

Stratigraphic analysis of the stacked section of IT-EG08B (Fig. 2) shows that R4 marks a significant change in the seismic character of the sedimentary succession (see also Rebesco et al., 2012). The sedimentary succession below this reflection appears relatively homogeneous in terms of amplitude and continuity, while above R4 the reflections display significant variations in amplitude. In this upper part, high-amplitude and laterally-continuous reflections alternate with lenses characterized by low-amplitude and discontinuous reflections. In particular, the reflection continuity is interrupted twice by the presence of the two MTDs PLS-1, and PLS-2. Above R4, only the eastern part of the MTD PLS-1 is imaged by our seismic profile, which shows its abrupt eastward lateral termination. PLS-2 is elongated, and its eastern (landward) part is contained in another seismic profile, not considered in this work (Llopart et al., 2014, 2015). Both MTDs consist of chaotic reflections with minor internal coherent reflectivity and show the presence of many diffractions. However, some internal reflectivity is present in these bodies, especially in the upper part of PLS-1 and within PLS-2. The thickness of the MTDs can reach 280 ms in the westernmost portion of PLS-1. Both MTDs show a lenticular-shaped geometry with a convex-up irregular upper bounding surface (Fig. 2).

4.2. Tomographic velocity field

P-wave (V_p) velocities resulting from the travel time inversion vary from about 1468 m/s of the sea-water to about 2420 m/s of the deepest layer (Fig. 4). The velocity in the first layer below the sea-floor is between 1750 and 1900 m/s. The V_p model shows a positive gradient with depth, with relatively high lateral velocity gradients. In particular, PLS-2 shows lateral variations with values ranging from 1860 to ~1750 m/s in the interval from 40 to 75 km from the start of the line (Fig. 4). PLS-1 has lateral variations of V_p from ~2360 to 2250 m/s, proceeding from left to right, from 0 to about 15 km from the start of the line on Fig. 4.

4.3. Sedimentary structure

In the pre-stack depth migrated section (Fig. 5A), the shallowest reflections appear better defined compared to the stacked section (Fig. 2), and most of the diffractions disappear. Moreover, the migration better details the internal features of the MTD bodies. Their boundaries are clearly marked (Fig. 5B), showing an irregular and local step-like character. Figs. 6 and 7 show the tomographic velocity field superimposed on the prestack depth migrated section, zoomed on PLS-1 and PLS2, respectively. Notwithstanding chaotic seismic facies characterize PLS-1 and PLS-2, some reflections could suggest the presence of internal layering. We performed several predictive deconvolution tests to analyse the nature of these reflections, by considering two representative subsets of the pre-stack depth migrated section in correspondence of the two MTDs (Fig. 8). In both MTDs the internal reflections disappear after deconvolution, proving that there are no internal structures. Therefore, the reverberations are probably due to a high impedance contrast between the MTDs and the embedding sediments.

The main body of PLS-1 terminates eastward (upslope) at about 17 km from the start of the line, although a thin toe (in the sense of Frey Martinez et al., 2005) extends up to 20 km from the start of the line.

The velocity field within PLS-2 (Fig. 7A) shows a slight V_p reduction (100–150 m/s) between about 60 to 80 km from the start of the line,

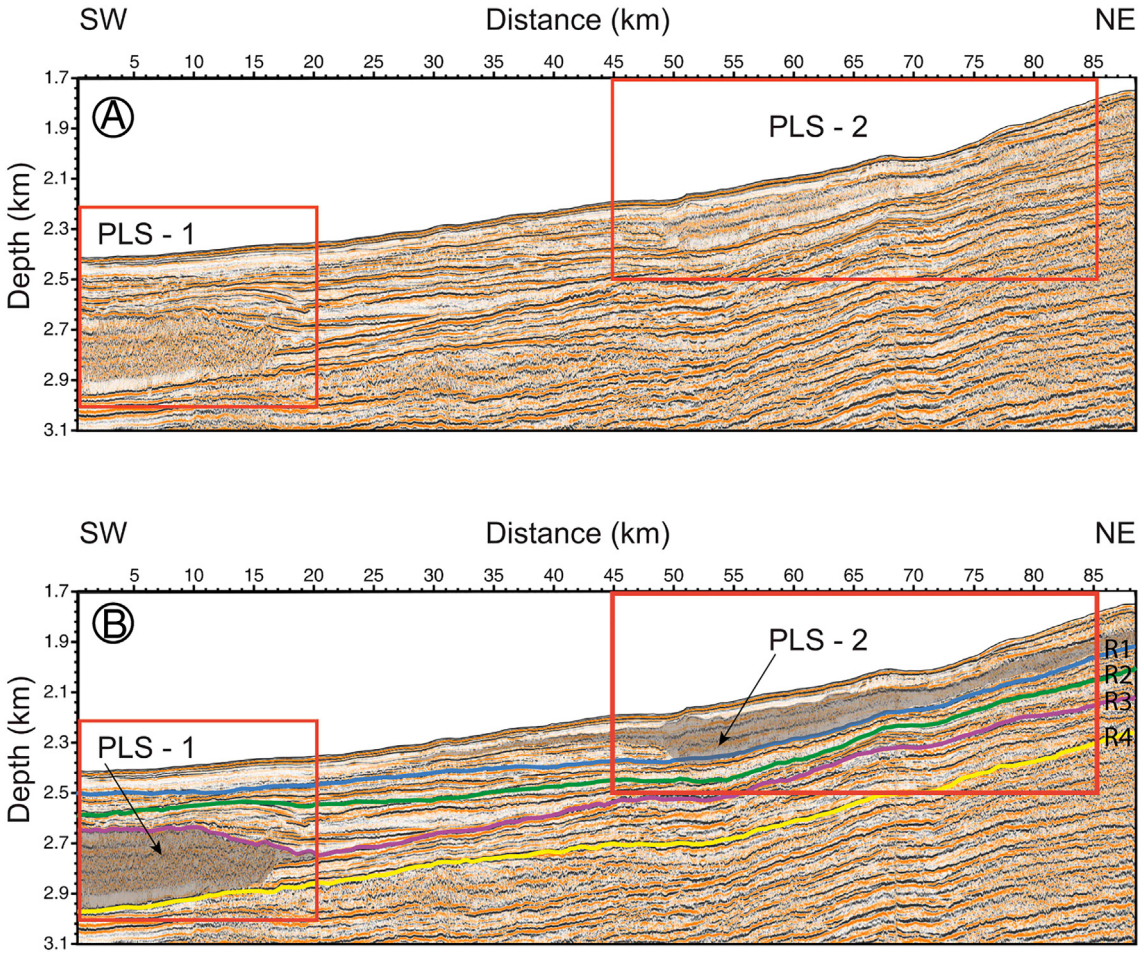

Fig. 5. Profile IT-EG08B. A) Prestack-depth migrated section. B) The same with the picked horizons shown in Fig. 2. The two giant MTDs are highlighted in grey. The red squares indicate the areas of the zooming of Figs. 6 and 7. (For interpretation of the references to color in this figure legend, the reader is referred to the web version of this article.)

where the average velocity is 1810 m/s. The main body of PLS-2 is identified between 49 and 68 km from the start of the line. West of it, there is a long, thin frontally emergent toe up to about 45 km from the start of the line (Fig. 7B). To the east, there is a transitional change, first to a sector where the MTD thins out (68–71 km from the start of the line), then to a sector with enhanced internal reflectivity (71–76 km from the start of the line), and finally to a sector (from 76 km to 88 km from the start of the line) where the MTD thickness is nearly half of the thickest part of the main body. The thickness in the imaged portion of seismic section reaches 340 m.

4.4. Instantaneous seismic attributes

The instantaneous amplitude and phase did not provide significant information. The instantaneous amplitude section is characterized by alternations of high-amplitude reflections and low-amplitude bands, while the instantaneous phase plot shows a general bedding continuity, interrupted by the two MTDs.

The instantaneous frequency section, on the contrary, reveals some interesting features (Fig. 9). There is a general reduction of the frequency with depth. However, this change appears to be not gradual, and it mainly occurs in association with reflection R3. In the uppermost part of the section, we note relatively low frequencies at 2500 m depth and 10–12 km (from the start of the line), and at about 2200 m depth and about 70 km (from the start of the line). The frequency content within both MTDs is characterized by homogeneous and significantly lower values (in average 45 Hz for PLS-1 and 60 Hz for PLS-2) with respect to the surrounding sediments.

4.5. Tomographic attenuation field

The depth distribution of the quality factor Q_p between horizons R1–R4, shows high variability, both laterally and vertically, with values ranging from 50 to 240 (Fig. 10). The highest values are more frequent in the deepest layer. The average Q_p value of the local sediments at the sea bottom is about 60.

The uppermost layer shows an upslope Q_p increase from about 150 to 200 units from the toe to the main body of PLS-2, with an average value of 190. The two intermediate layers are characterized by lower values (50–171), with both layers showing downslope decreasing values. The minimum value (50) is at a depth of 2520 m and between 4 and 16 km from the start of the line. The maximum value is observed above the eastern edge of PLS-1, between 17 and 21 km from the start of the line, at about 2640 m depth.

The lowermost layer shows a lateral variation of Q_p values from 89 to 238, not correlated with depth; the highest values are present both in the north-eastern part as well as south-westwards in the PLS-1 MTD body. The lateral boundary of PLS-1 is marked by a sharp variation of Q_p values at ~17 km from the start of the line, changing from 151 outside the MTD to ~238 inside it, with an average value of 210 within the MTD.

4.6. Rock physics and porosity field

A velocity-porosity function was computed using the generalized Gassmann model and the petrophysical parameters of Table 1. We found that a value A = 4 for the exponential coefficient in the Krief

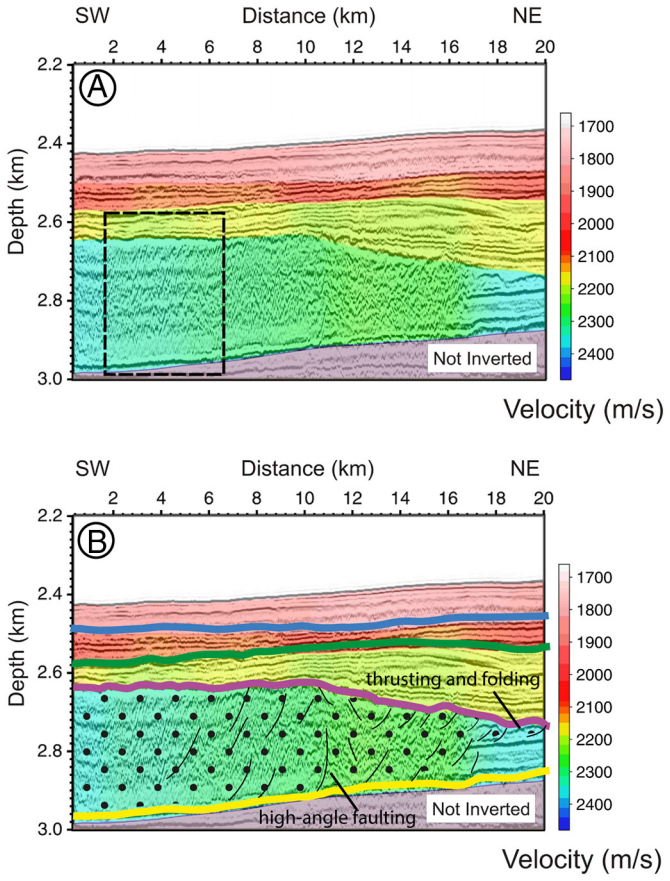

Fig. 6. Profile IT-EG08B zoomed on PLS-1 (see in Fig. 5B the location with respect to the entire line). A) Tomographic velocity field superimposed on the prestack depth migrated section. The dashed rectangle indicates the limits of the subset used for the deconvolution test of Fig. 8. B) The same as A, with the picked horizons, the MTD evidenced with dots, and some interpreted features. The easternmost part of the MTD is characterized by lateral ramps, associated with thrust folds and flower structures. X-axis: distance from the start of the line (SW) in km. Y-axis: depth (km).

relationship provides the best match (Fig. 11) between the computed function and the velocity-porosity values obtained from the sonic-log at ODP Site 986 (Table 17 in Jansen et al., 1996). This value reflects the fact that the pores are crack-like because of the high clay content (Le Ravalec and Guéguen, 1996).

The porosity field calculated using the derived velocity-porosity function shows values between 23 and 42% (Fig. 12). Modeling results reveal a decrease in porosity with depth, as expected, together with lateral variations. The MTD PLS-1 is characterized by porosity values ranging from 26 to 30% (Fig. 12), with the highest values towards its eastern edge. For PLS-2 the porosity varies from about 37 to 42% upslope (Fig. 12).

4.7. A focus on the two MTDs

In the following, we shortly summarize the main results of the different methodologies, with an emphasis on the two MTDs. For this scope, velocity, Q_p, and porosity values are plotted in Fig. 13 for MTD PLS-1 (a, c, e) and PLS-2 (b, d, f).

In PLS-1, a decrease of velocity is observed from the start of the line to 13 km from it, followed by an increase towards the NE margin of the MTD (Fig. 13a). The porosity trend is necessarily opposite (Fig. 13c), with values varying from 26% to 29%, while Q_p initially decreases of about 50 units towards 5 km from start of the line, then there is an increase of 20 units from 5 to 12 km from the start of the line, and a new decrease of 80 units towards the NE margin of the MTD (Fig. 13e).

In PLS-2, the velocity increases of 70 m/s at about 50 km from the start of the line (Fig. 13b) where the highest thickness of the deposit is observed (Fig. 7). Upslope the values decrease by 135 m/s from 50 to 66 km from the start of the line. A flat area is observed for about 11 km, in correspondence of two zones of disturbance (Fig. 7), followed by a new velocity increase of 95 m/s towards the end of the line (Fig. 13b). The porosity values are in the interval 37%–41% (Fig. 13d). As regards as Q_p factor, a positive upslope trend characterizes the values starting from the toe towards the main body of the MTD, with an increase of 50 units in the interval 45–61 km from the start of the line. A decrease of 30 units characterizes the range 61–74 km from the start of the line.

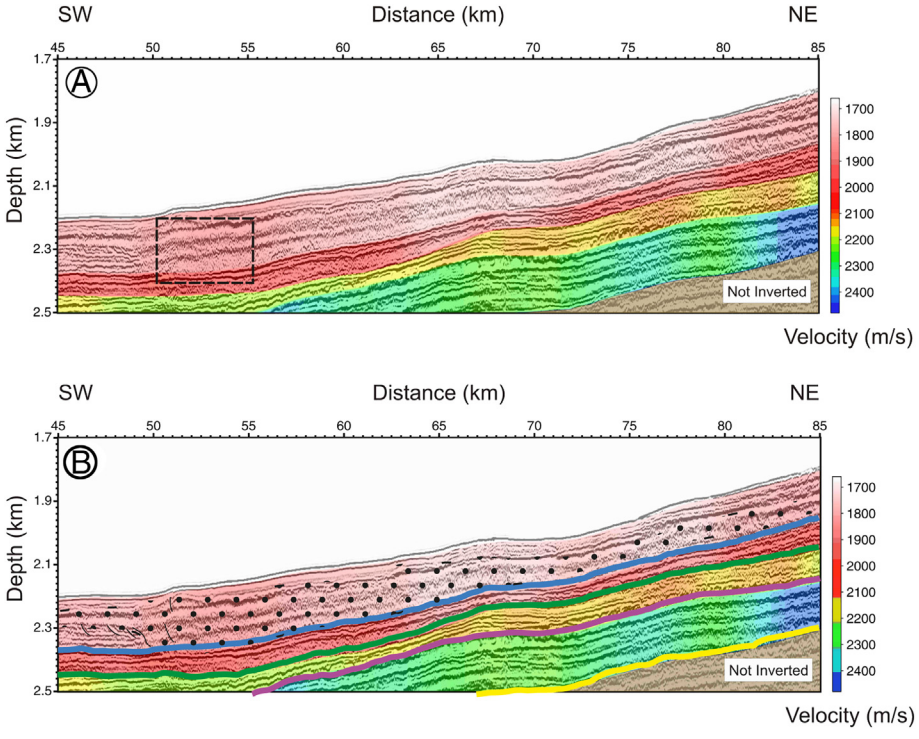

Fig. 7. Profile IT-EG08B zoomed on PLS-2 (see in Fig. 5 the location with respect to the entire line). A) Tomographic velocity field superimposed on the prestack depth migrated section. The dashed rectangle indicates the limits of the subset used for the deconvolution test of Fig. 8. B) The same as A, with the picked horizons, the MTD evidenced with dots, and some interpreted features. The MTD is characterized by semi-transparent to chaotic acoustic reflectors sub-parallel to the slope. X-axis: distance from the start of the line (SW) in km. Y-axis: depth (km).

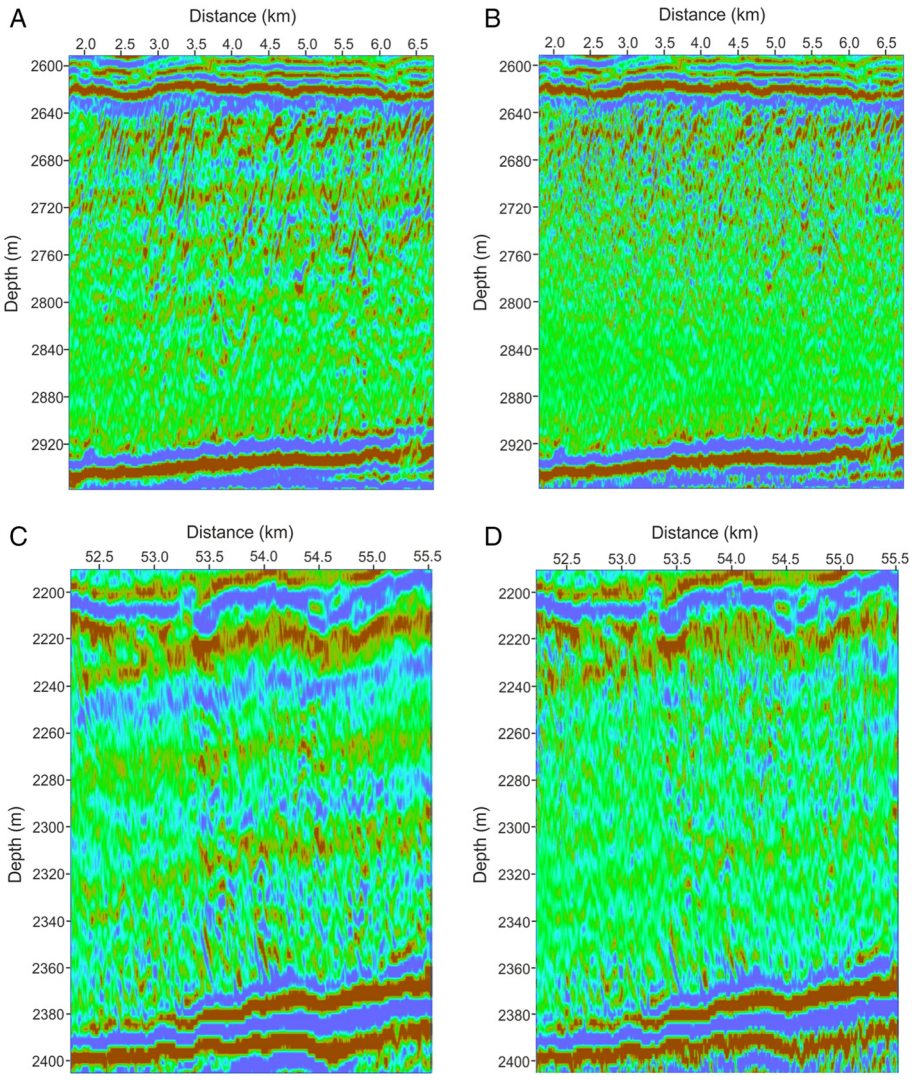

Fig. 8. A test of deconvolution on the subsets indicated in Figs. 6 and 7. A) PLS1-subset before the deconvolution, and B) after it: prediction length 20 m; operator length 200 m. C) PLS2-subset before the deconvolution, and D) after it: prediction length 10 m; operator length 100 m. These operators are designed only for the two MTDs. Their application outside the MTDs generates artifacts as, e.g., at the bottom right corner of panel D.

A new increase of 50 units is observed from here to the end of the line (Fig. 13f).

A further difference between the two MTDs regards their clay content. We computed all the possible values of porosity and clay content which allow a simultaneous match of average P-wave velocity and quality factor for PLS-1 (V_p = 2300 ± 70 m/s and Q_p = 210 ± 12 at a dominant frequency f = 45 Hz) and for PLS-2 (V_p = 1810 ± 80 m/s and Q_p = 190 ± 20 at a dominant frequency f = 60 Hz). Fig. 14 shows all the points found for PLS-1 and PLS-2, where the average porosity is $\Phi_{av} = \Phi_1 p_1 + \Phi_2 p_2$. The most probable values characterizing the two MTDs are the barycentre of the clay content and porosity point clouds. The errors associated with the final values are the

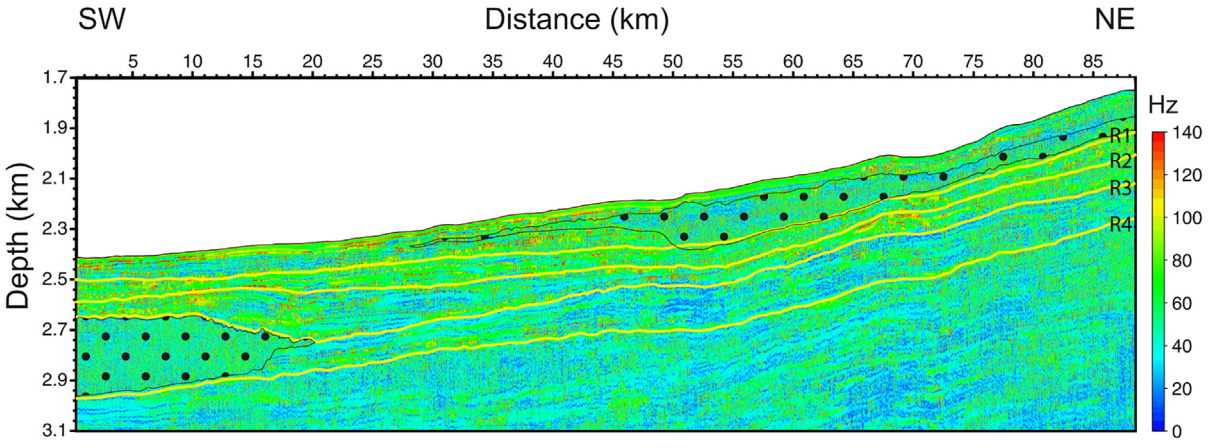

Fig. 9. Profile IT-EG08B. The instantaneous frequency of the prestack migrated section. The MTDs are evidenced by filling dots. X-axis: distance from the start of the line (SW) in km. Y-axis: depth (km).

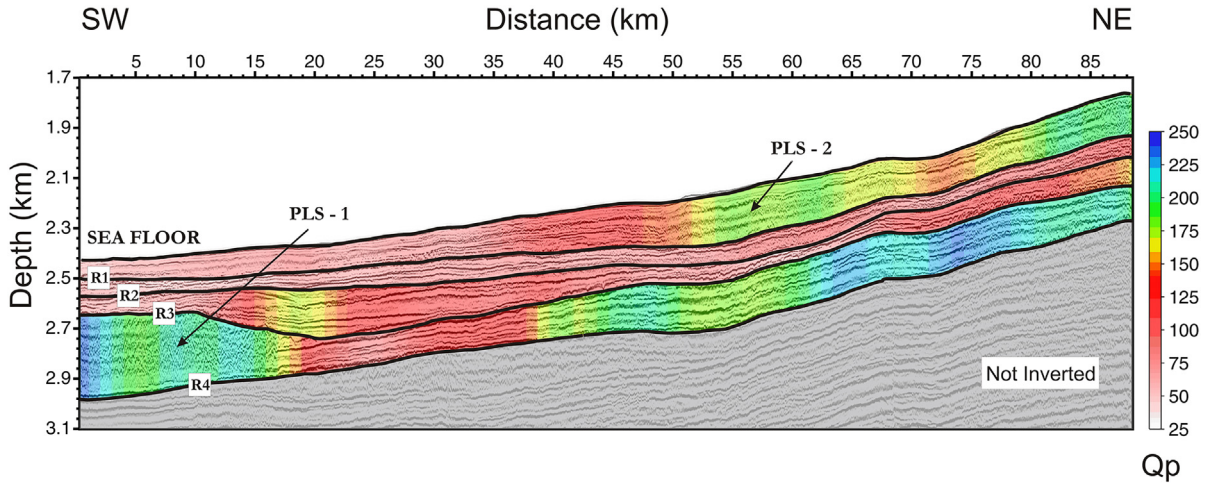

Fig. 10. Profile IT-EG08B. Seismic quality factor (Q_p) field superimposed on the prestack depth migrated section. The two MTDs analysed (PLS-1 and PLS-2) are indicated by arrows. X-axis: distance from the start of the line (SW) in km. Y-axis: depth (km).

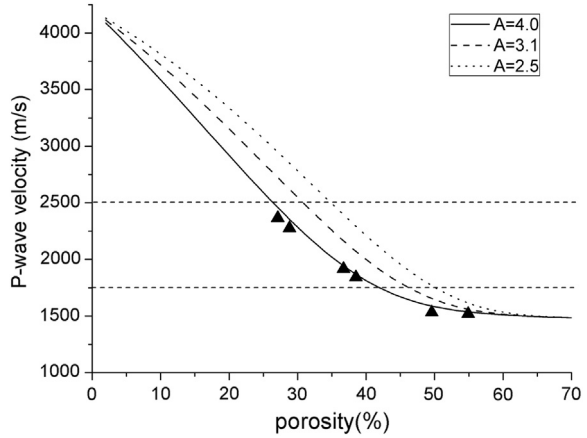

Fig. 11. Different curves representing porosity versus P-wave velocity, computed using the generalized Gassmann method, the physical properties reported in Table 1 and the results of the geotechnical measurements on the core samples at ODP Site 986 (Table 17 in Jansen et al., 1996). We tested for A (the Krief exponential coefficient - Carcione et al., 2005) the values 2.5, 3.1 and 4. The plot shows a good match between the computed function and the sonic-log velocity-porosity values obtained for A = 4 at different depths. The horizontal dashed lines indicate the P-wave velocity interval of our data.

corresponding standard deviations. The average porosities are 24 ± 5% and 33 ± 4% for PLS-1 and PLS-2, respectively. Similarly, the corresponding average clay contents are 39 ± 5% and 68 ± 6% for PLS-1 and PLS-2, respectively. Moreover, we can also find a difference in the grain size within the two MTDs. In fact, the size wavelength of the inhomogeneities that originate diffractions in a seismic stacked section is comparable with the wavelength of the seismic wave. In both MTDs, diffractions are observable (Figs. 6 and 7). Using the above average velocity and frequency values, for PLS-1 the wavelength of the disturbance is 51 ± 1.5 m, whereas for PLS-2 it is 30 ± 1.3 m. Thus, following the λ/4 criterion, the size of the inhomogeneities is about 12 m and 8 m in PLS-1 and PLS-2, respectively.

5. Discussion

5.1. Interpretation of observed features and seismic properties

The boundaries of the two MTDs present in section IT-EG08B are clearly delineated by the seismic data (Fig. 5B), showing their irregular and local step-like character. In the easternmost part of PLS-1, high-angle discontinuities are identifiable, which are interpreted as thrust and fold structures (Fig. 6B).

PLS-1 and PLS-2 are respectively located on the lower and mid-continental slope and are characterized by a thick chaotic and

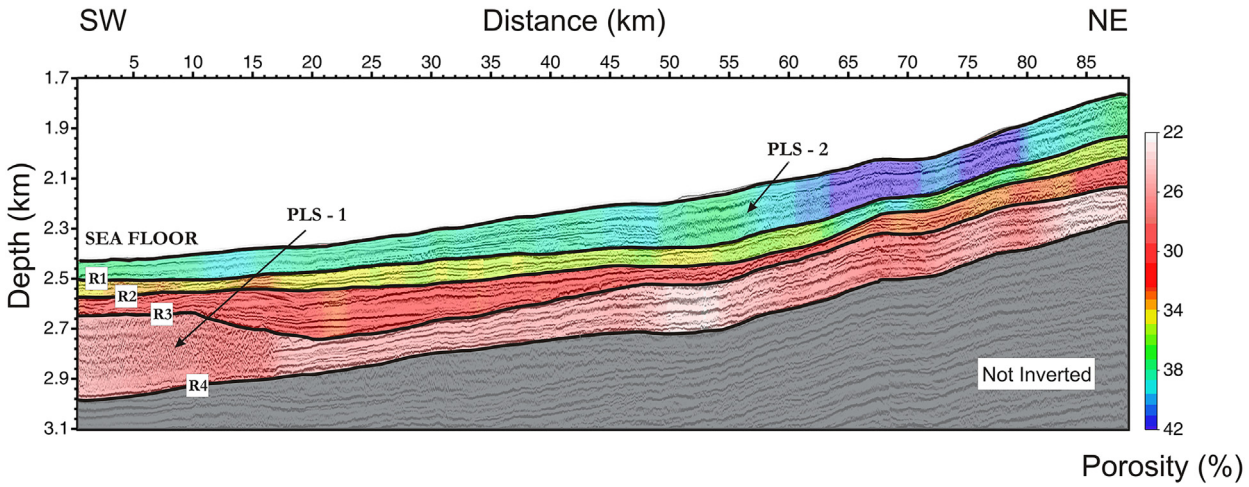

Fig. 12. Profile IT-EG08B. Porosity field superimposed on the prestack depth migrated section. The two MTDs analysed (PLS-1 and PLS-2) are indicated by arrows. X-axis: distance from the start of the line (SW) in km. Y-axis: depth (km).

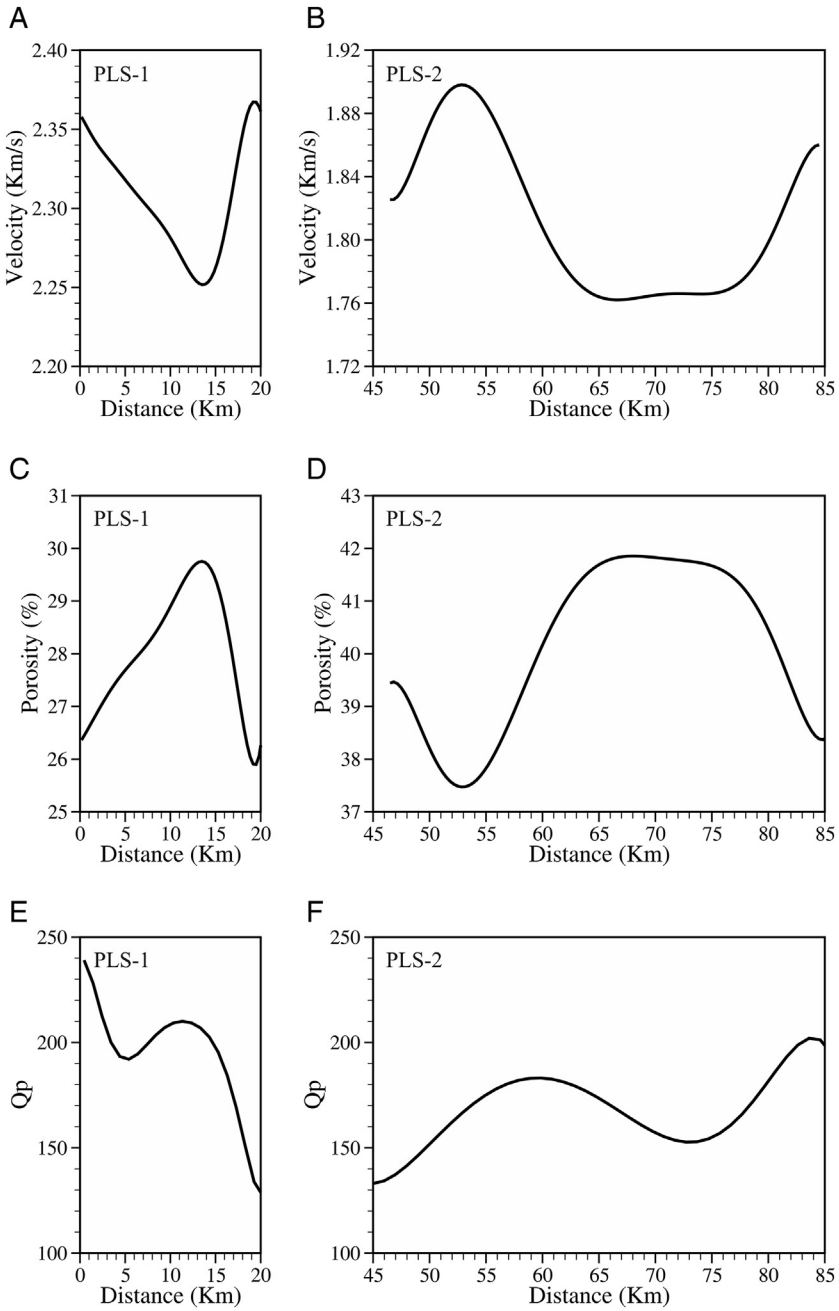

Fig. 13. V_p, porosity, and Q_p (Y-axis) versus the distance from the start of the line (X-axis) for PLS-1 (a, c, e) and PLS-2 (b, d, f). We considered the same subsets of Figs. 6 and 7.

fractured acoustic unit embedded within a sequence of thinner MTDs (which may be interpreted as glacigenic debris flow deposits) and glaciomarine sediments. This feature and the presence of deformed structures and diffractions imply scattering and phase interference of the seismic waves, resulting in lower resolution within the MTDs. The most remarkable characteristic of the MTDs in seismic data is, in fact, the instantaneous frequency, which is significantly lower and more homogeneous with respect to the hosting sediments (Fig. 9). The slightly smaller Q_p values above PLS-1 with respect to the values in the same layer are probably due to the scattering at the top of PLS-1, which causes a sudden loss of high-frequencies to the incident-wave and consequently also to the reflected and transmitted waves. Nevertheless, the Q_p and velocity values obtained for seismic profile IT-EG08B are in agreement with previous observations on the same margin with a wider offset range (Rossi et al., 2007; Westbrook et al., 2008; Kandilarov et al., 2010; Madrussani et al., 2010; Rajan et al., 2012). The validity of the velocity field obtained is verified through the quality of the migrated section (Fig. 5), where most of the diffractions present in Fig. 2 collapse in a single point. Moreover, the average Q_p value obtained at sea bottom is in agreement with the measured value of a core sample taken on the continental slope of the Barents Sea, at a water depth of 2227 m (Ayres and Theilen, 2001). Sediment compaction during burial, for de-watering effects, is highlighted by the increase of the velocity with depth (e.g., Fig. 4). This is consistent with the reduction of the instantaneous frequency and porosity with depth (Figs. 9 and 12). The instantaneous frequency variation, however, is not gradual, but occurring mainly in association with reflection R3 (Fig. 9), suggesting lithological variations (see Section 5.3).

The comparative analysis of velocity, Q_p factor, and porosity (Fig. 13) may allow interpreting the lateral variations of these three quantities in terms of lateral sediment distribution within an MTD. The main observations on the MTDs done on the stacked and migrated sections, completed with the main features from instantaneous

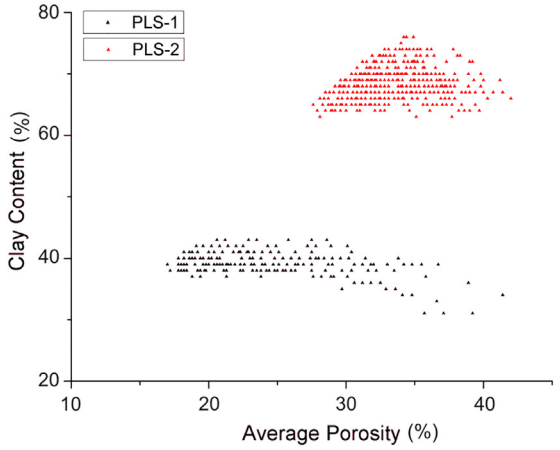

Fig. 14. Petrophysical analysis of PLS-1 and PLS-2 using White's model (White, 1975; White et al., 1975), showing the clay content (Y-axis) versus the porosity (X-axis). The black and red points represent all the possible values of porosity and clay associated to PLS-1 and PLS-2, respectively, satisfying the average tomographic values V_p and Q_p within the estimated value uncertainty (see text). The barycentre coordinates (clay content and porosity) of the two point clouds is assumed to represent the most probable values characterizing the two MTDs. X-axis: porosity (%). Y-axis: clay content (%). (For interpretation of the references to color in this figure legend, the reader is referred to the web version of this article.)

frequency analysis, and traveltime and attenuation tomography, are summarized in Fig. 15.

The thickness of PLS-2 is quite variable, from 60 m to 180 m in the main body, thinning to 45 m in the toe. The proximal part of PLS-2 is comparatively thin and characterized by relatively high seismic velocity and attenuation and by lower porosity, suggesting highly compacted sediments (> 80 km from the start of the line, star in Fig. 15B). In this part of the MTD, the thickness is about 50–60% of the modeled layer, so we cannot exclude a contribution of the overlying sediments in our results. In fact, having picked the reflected waves from the top and bottom of each layer, V_p can vary only horizontally within each layer and represents a value averaged on the whole layer thickness.

The eastern part of the main body (60–70 km from the start of the line) is probably composed of less compacted and relatively softer sediment, with higher porosity (square in Fig. 15B). Then, proceeding downslope towards the main body of the MTDs, the sediment progressively reduces its porosity and consequently the consolidation increases (50–60 km from the start of the line, star in Fig. 15B). Here the values are representative of the MTD since its thickness varies between 70 and 86% of that of the layer. Talling et al. (2007) described a complex transition between different flow types (turbidite to debrite and vice-versa), from the exit ramp to the toe of the MTD, under the influence of different sea-floor gradients. The seismic response of PLS-2 is consistent throughout the profile, indicating that such changes in flow type did not occur in the area, despite small variations in slope gradient. Nevertheless, such small variations in the slope gradient could have affected the flow dynamics resulting in parts of the deposit that stretched or compressed producing differences in porosity characteristics.

The Q_p factor analysis also indicates the presence of fluids (possibly gas) near the toe of PLS-2 (40–50 km from start of the line, circle in Fig. 15B). Because the Q_p, V_p, and porosity relate to the whole thickness of the layer between the sea-floor and R1 and because PLS-2 significantly thins at its toe to about 30% of the layer, we think that the low Q_p and high porosity values are rather related to high content of fluid in the sediments underlying the toe of the MTD. In contrast to the generally observed decrease in the interparticle porosity in MTDs, particularly at their base (Urgeles et al., 2006; Sawyer et al., 2009; Strasser et al., 2012), here the average porosity is relatively high, especially for PLS-2. The velocity changes observed within both MTDs (Figs. 4, 6, 7) can be due to the presence of unsorted or chaotic deposits, changes in porosity, and variable fluid content.

5.2. Main differences in the compaction of two MTDs

There are, however, differences in the two MTDs that it is worth analysing in more detail. Our analysis confirms that in the case of PLS-2, profile IT-EG08B strikes approximately along the flow direction, so that we have a longitudinal section of the MTD, while in the case of PLS-1 the profile is inferred to cross the MTD body obliquely, at an undefined distance from its frontal part (Rebesco et al., 2012).

In PLS-2, we observe lateral changes in Q_p, V_p, and porosity. Such lateral changes can be due to vertical and lateral variations of lithology, cementation, porosity, density and, hence, compaction (e.g., Kim et al., 2001). De-watering and compaction of the sediments could be responsible for the porosity values observed in the main body (Fig. 12). It has been shown that MTDs exhibit reduced intergranular porosity and increased shear strength compared to bounding sediments (Urgeles et al., 2006; Sawyer et al., 2009; Strasser et al., 2012). Sawyer et al. (2009) interpreted the decreased intergranular porosity within the MTDs in terms of uniaxial vertical consolidation during the burial of an MTD that had been “remoulded” during transport as a debris flow.

In PLS-1, the comparison of the Q_p, velocity and porosity values suggests that the variation trend is inverse to the one observed near the toe of PLS-2 (Fig. 13). In fact, at the SW limit of the sections, i.e., within the main body, there is a relatively high Q_p and velocity with low porosity, an indication of highly compacted sediments (< 5 km from the start of the line; star in Fig. 15B). In fact, this MTD region appears to have been subject to significant compression, a process that reduces the length of the MTD and increases its thickness. Lateral ramps, associated with thrust-folding and transpressional structures are recognizable in the migrated section (Fig. 6), associated with a slight velocity reduction (about 100 m/s). Since for PLS-1 the porosity is lower than 40%, we can assume that the velocity mainly reflects to porosity changes (also due to fracturing) because the rock is stiffer, i.e., the dry-rock bulk modulus is higher (Nur et al., 1995; Sallarès and Ranero, 2005). The fractures inside the MTD are interpreted to result from lateral friction with the surrounding sediments during the sliding. Moving to the east, towards the MTD lateral boundary, the material becomes less compacted and relatively softer, with higher porosity (5–12 km from the start of the line, circle in Fig. 15B), maybe due to fracturing.

5.3. Modeled lithologies as a proxy for source area

With respect to PLS-2, PLS-1 shows higher velocities, and lower porosity, in agreement with its greater burial depth and consequent sediment compaction. Such values may, however, also be related to the grain size composition.

The petrophysical analysis carried out for PLS-1, and PLS-2 indicates that the MTDs have a relatively high clay content, comparable to that of the sediments in the ODP Site 986 (56%, see Table 1). In particular, PLS-1 shows clay content of nearly 40%, whereas PLS-2 shows clay content of about 65% (Fig. 14). In the two MTDs, the higher clay content with respect to the surrounding sediments results in average porosities that are lower than those already computed using the generalized Gassmann's method. Furthermore, the noticeable difference in the clay content and grain size between the two MTDs is inferred to relate to their different source areas.

PLS-2, which shows higher clay content and hence finer average grain size, is interpreted by Rebesco et al. (2012) to come from the northern flank of the Kveithola TMF, with a run-out distance of about 90 km. This area, in between the major Storfjorden and Bjørnøya TMFs, is characterized by fine-grained sediments (mainly plumites and hemipelagites with high pore fluid and clay content) and this fact is consistent with our results. From section IT-EG08B alone (Fig. 5), it is not possible to measure the elevation difference between the head scarp

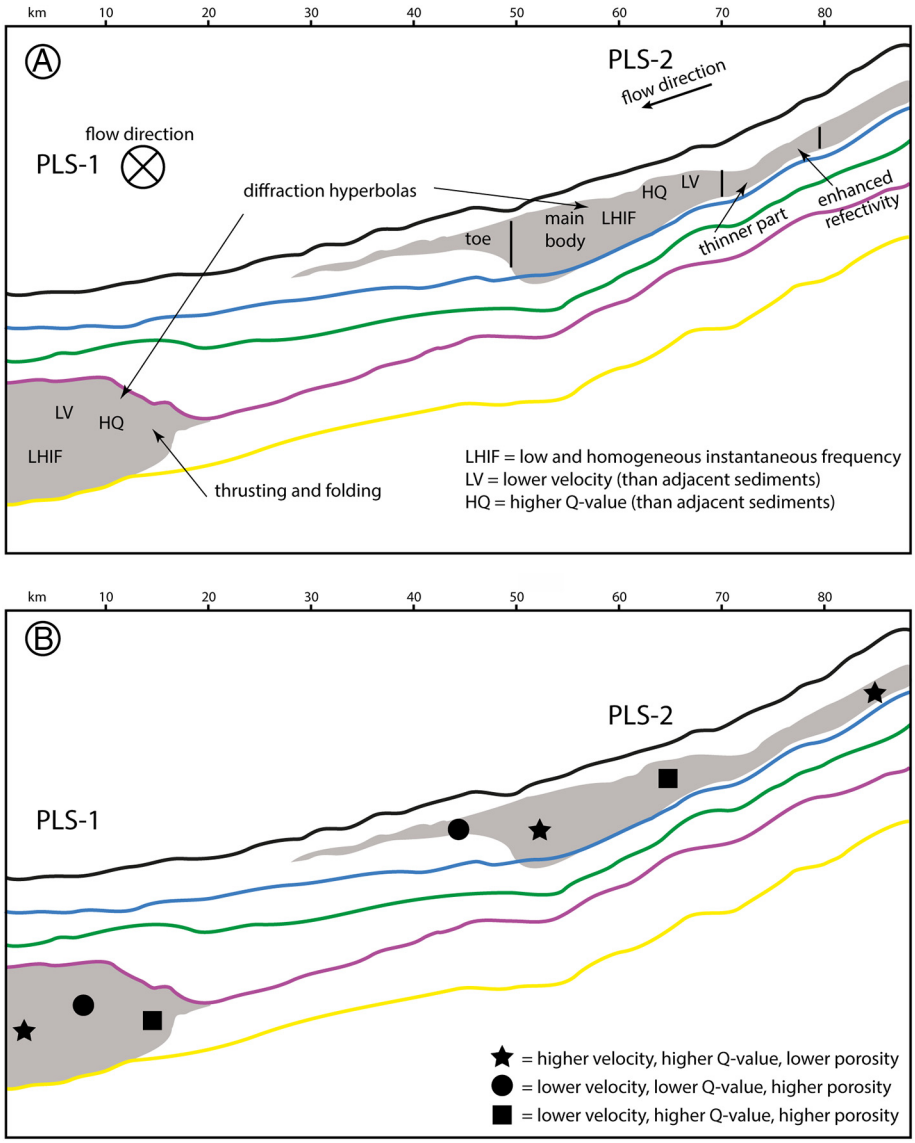

Fig. 15. Summary sketch outlining the internal attributes of the two studied MTDs on a line drawing of the considered reflectors. A) Characteristics of both MTDs with respect to the surrounding sediments. The principal subdivisions of PLS-2 are shown. The presence of diffraction hyperbolas, thrusting and folding, and enhanced reflectivity are indicated. The inferred flow directions are also reported. B) Distribution of internal properties (shown with symbols) within the two MTDs.

and the toe of the MTD. However, based on the conclusions in Rebesco et al. (2012), and on the data herein presented, we can estimate it to be 750 m.

Conversely, PLS-1, which shows lower clay content and simultaneous presence of coarser sediments, is inferred to have originated from the southern part of the Storfjorden TMF or from the northern part of the Bjørnøya TMF, where glacigenic debris flows are predominant. We prefer the latter hypothesis since this large MTD lies just in front of the Bjørnøya TMF, which is the largest TMF in the area. If so, the minimal run-out distance that we can estimate is approximately 170 km, considering the distance between the point where seismic profile IT-EG-08 intersects the MTD and the shelf edge of the northern part of Bjørnøya TMF, from where PLS-1 may have detached. Flume experiments show that in gravity flows with a clay content exceeding 15%, as it is the case for these MTDs, the run-out distance decrease with increasing clay content (Ilstad et al., 2004). Hence, the lower clay content of the PLS-1 could contribute to its larger run-out. Due to the different orientation of the flow with respect to the strike of the seismic profile, it is not possible to measure the elevation difference between the scarp and the toe of the PLS-1.

6. Conclusions

Different analytical techniques were applied to a multichannel seismic reflection profile recorded off the Kveithola TMF, to infer the distribution, petrophysical properties and origin of the sediments composing two MTDs located at an average depth of about 2.1 and 2.8 Km, respectively.

Velocity estimation derived by tomographic inversion of travel times identified lateral velocity anomalies that we infer to be associated with significant variations in sediment parameters. Amongst them, the occurrence of low-velocity zones related to MTDs is indicative of deformation due to the downward displacement of the sediment mass (Fig. 4). Seismic attributes, or at least the instantaneous frequency, represent a useful tool to characterize the geometry of the different MTDs (Fig. 9). The comparative analysis of P-wave quality factor values (Q_p), velocity and porosity, supported by rock-physics theories and integrated with the geometrical interpretation of the MTDs, provide new insights on the lithology and, therefore, on the possible origin of the two MTDs. PLS-1 is estimated to have a lower fluid content and higher strength with respect to PLS-2 since it has higher velocity (Fig. 6 and for comparison Fig. 7), lower porosity (Fig. 13), and higher instantaneous frequency (Fig. 9). These differences are likely mainly due to the age

and burial depth, but source area effects cannot be discarded. In fact, the inferred coarser sediment in PLS-1 (clay content of nearly 40%, Fig. 14) could suggest a provenance from areas with abundant glacigenic debris flows. These conditions may be possibly consistent with a sediment source from a TMF, likely the Bjørnøya TMF. PLS-2, on the other hand, is characterized by finer sediments (clay content of about 65%), relatively high fluid content, shorter translation, lower velocity (Fig. 7), and lower instantaneous frequency (Fig. 9). This could support the interpretation of Rebesco et al. (2012) that PLS-2 originated from the northern flank of the Kveithola TMF, an area in between the major Storfjorden and Bjørnøya TMFs, where the glacier was slower moving, and where there is a relatively more significant production of turbidites, plumites and hemipelagites.

The results of this study demonstrate that the use of velocity and attenuation tomographic inversion, together with advanced processing, attribute analysis and modeling of physical properties may help to investigate and reconstruct the sediment deposition and post-deposition processes in areas affected by submarine MTDs, also with scarcity of seismic profiles and in the absence of nearby borehole measurements in the study area. This methodology can hence be used for a preliminary planning of offshore infrastructures and assessment of risk management in areas where MTDs have been identified on a limited seismic dataset.

Acknowledgements

We wish to thank the entire staff that supported the OGS IPY Project EGLACOM. The Italian contribution was funded by the PNRA project VALFLU and by the ARCA project. Spanish participants were funded by the Spanish projects DEGLABAR (CTM2010-17386) and CORIBAR-ES (CTM2011-14807-E) funded by the "Ministerio de Economia y Competitividad". The "Generalitat de Catalunya" is acknowledged for support through an excellence research group grant (2014SGR940). J.L. was funded by an FPI grant BES-2011-043614. Pre-stack depth migration processing and the computation of complex seismic were carried out with the Seismic Unix software package (Stockwell, 1997). Tomographic inversion was performed by using the software package CAT-3D developed at OGS (http://www.3dtomography.com). We are in debt to Flavio Accaino, Gualtiero Böhm and Davide Gei for the fruitful and stimulating discussions that helped as background to the writing of this article. We thank the editor Gert De Lange, Tiago M. Alves and the other anonymous reviewers for the constructive comments that helped us to improve our manuscript significantly.

Appendix A. Supplementary data

Supplementary data to this article can be found online at https://doi.org/10.1016/j.margeo.2017.11.013.

References

Alves, T.M., Kurtev, K., Moore, G.F., Strasser, M., 2014. Assessing the interval character, reservoir potential, and seal competence of mass-transport deposits using seismic texture: a geophysical and petrophysical approach. AAPG Bull. 98 (4), 793–824. http://dx.doi.org/10.1306/09121313117.

Anwar, H.M., Ali, A., Alves, T.M., 2017. Bayesian inversion of synthetic AVO data to assess fluid and shale content in sand-shale media. J. Earth Syst. Sci. 126 (42), 1–13. http://dx.doi.org/10.1007/s12040-017-0818-y.

Ayres, A., Theilen, F., 2001. Preliminary laboratory investigations into the attenuation of compressional and shear waves on near-surface marine sediments. Geophys. Prospect. 49 (1), 120–127. http://dx.doi.org/10.1046/j.1365-2478.2001.00243.x.

Baeten, N.J., Laberg, J.S., Vanneste, M., Forsberg, C.F., Kvalstad, T.J., Forwick, M., Vorren, T.O., Haflidason, H., 2014. Origin of shallow submarine mass movements and their glide planes - sedimentological and geotechnical analyses from the continental slope off northern Norway. J. Geophys. Res. F: Earth Surf. 119 (11), 2335–2360. http://dx.doi.org/10.1002/2013JF003068.

Batzle, M., Wang, Z., 1992. Seismic properties of pore fluids. Geophysics 57 (11), 1396–1408. http://dx.doi.org/10.1190/1.1443207.

Böhm, G., Carcione, J.M., Gei, D., Picotti, S., Michelini, A., 2015. Cross-well seismic and electromagnetic tomography for CO_2 detection and monitoring in a saline aquifer. J. Pet. Sci. Eng. 133, 245–257. http://dx.doi.org/10.1016/j.petrol.2015.06.010.

Bugge, T., Befring, S., Belderson, R.H., Eidvin, T., Jansen, E., Kenyon, N.H., Holtedahl, H., Sejrup, H.P., 1987. A giant three-stage submarine slide off Norway. Geo-Mar. Lett. 7 (4), 191–198. http://dx.doi.org/10.1007/BF02242771.

Butt, F.A., Elverhøi, A., Solheim, A., Forsberg, C.F., 2000. Deciphering late Cenozoic development of the western Svalbard margin from ODP Site 986 results. Mar. Geol. 169 (3–4), 373–390. http://dx.doi.org/10.1016/S0025-3227(00)00088-8.

Carcione, J.M., Picotti, S., 2006. P-wave seismic attenuation by slow-wave diffusion: effects of inhomogeneous rock properties. Geophysics 71 (3), O1–O8. http://dx.doi.org/10.1190/1.2194512.

Carcione, J.M., Helle, H.B., Santos, J.E., Ravazzoli, C.L., 2005. A constitutive equation and generalized Gassman modulus for multimineral porous media. Geophysics 70 (2), n17–n26. http://dx.doi.org/10.1190/1.1897035.

Chiocci, F.L., Cattaneo, A., Urgeles, R., 2011. Seafloor mapping for geohazard assessment: state of the art. Mar. Geophys. Res. 32 (1), 1–11. http://dx.doi.org/10.1007/s11001-011-9139-8.

Diviacco, P., Rebesco, M., Camerlenghi, A., 2006. Late Pliocene mega debris flow deposit and related fluid escapes identified on the Antarctic peninsula continental margin by seismic reflection data analysis. Mar. Geophys. Res. 27, 109–128. http://dx.doi.org/10.1007/s11001-005-3136-8.

Donda, F., O'Brien, P.E., De Santis, L., Rebesco, M., Brancolini, G., 2008. Mass wasting processes in the Western Wilkes Land margin: possible implications for East Antarctic glacial history. Palaeogeogr. Palaeoclimatol. Palaeoecol. 260 (1–2), 77–91. http://dx.doi.org/10.1016/j.palaeo.2007.08.008.

Dondurur, D., Çifçi, G., 2007. Acoustic structure and recent sediment transport processes on the continental slope of Yeşilirmak River fan, Eastern Black Sea. Mar. Geol. 237 (1–2), 37–53. http://dx.doi.org/10.1016/j.margeo.2006.10.035.

Dowdeswell, J.A., Elverhøi, A., 2002. The timing of initiation of fast-flowing ice streams during a glacial cycle inferred from glacimarine sedimentation. Mar. Geol. 188 (1–2), 3–14. http://dx.doi.org/10.1016/S0025-3227(02)00272-4.

Dowdeswell, J.A., Kenyon, N.H., 1995. Long-range Side-scan Sonar Investigations of the Polar North Atlantic: Patterns and Processes of Sedimentation on a Glaciated Passive Continental Margin. Cruise Report 95-01: R.R.S. James Clark Ross Cruise 08. Report. University of Wales, Aberystwyth.

Dowdeswell, J.A., Elverhøi, A., Spielhagen, R., 1998. Glacimarine sedimentary processes and facies on the Polar North Atlantic margins. Quat. Sci. Rev. 17 (1–3), 243–272. http://dx.doi.org/10.1016/S0277-3791(97)00071-1.

Dumke, I., Burwicz, E.B., Berndt, C., Klaeschen, D., Feseker, T., Geissler, W.H., Sarkar, S., 2016. Gas hydrate distribution and hydrocarbon maturation north of the Knipovich Ridge, western Svalbard margin. J. Geophys. Res. Solid Earth 121 (3), 1405–1424. http://dx.doi.org/10.1002/2015JB012083.

Faleide, J.I., Solheim, A., Fiedler, A., Hjelstuen, B.O., Andersen, E.S., Vanneste, K., 1996. Late Cenozoic evolution of the western Barents Sea-Svalbard continental margin. Glob. Planet. Chang. 12 (1–4), 53–74. http://dx.doi.org/10.1016/0921-8181(95)00012-7.

Fiedler, A., Faleide, J.I., 1996. Cenozoic sedimentation along the southwestern Barents Sea margin in relation to uplift and erosion of the shelf. Glob. Planet. Chang. 12 (1–4), 75–93. http://dx.doi.org/10.1016/0921-8181(95)00013-5.

Forsberg, C.F., Solheim, A., Elverhøi, A., Jansen, E., Channell, J.E.T., Andersen, E.S., 1999. The depositional environment of the western Svalbard margin during the late Pliocene and the Pleistocene: sedimentary facies changes at Site 986. In: Raymo, M.E., Jansen, E., Blum, P., Herbert, T.D. (Eds.), Proc. ODP, Sci. Results, 162: College Station, TX (Ocean Drilling Program), pp. 233–246. http://dx.doi.org/10.2973/odp.proc.sr.162.032.1999.

Frey Martinez, J., Cartwright, J., Hall, B., 2005. 3D seismic interpretation of slump complexes: examples from the continental margin of Israel. Basin Res. 17 (1), 83–108. http://dx.doi.org/10.1111/j.1365-2117.2005.00255.x.

Gales, J.A., Leat, P.T., Larter, R.D., Kuhn, G., Hillenbrand, C.-D., Graham, A.G.C., Mitchell, N.C., Tate, A.J., Buys, G.B., Jokat, W., 2014. Large-scale submarine landslides, channel and gully systems on the southern Weddell Sea margin, Antarctica. Mar. Geol. 348 (1), 73–87. http://dx.doi.org/10.1016/j.margeo.2013.12.002.

Hanebuth, T.J.J., Rebesco, M., Urgeles, R., Lucchi, R.G., Freudenthal, T., 2014. Drilling glacial deposits in offshore polar regions. Eos 95 (31), 277–278. http://dx.doi.org/10.1002/2014EO310001.

Hjelstuen, B.O., Elverhøi, A., Faleide, J.I., 1996. Cenozoic erosion and sediment yield in the drainage area of the Storfjorden fan. Glob. Planet. Chang. 12 (1–4), 95–117. http://dx.doi.org/10.1016/0921-8181(95)00014-3.

Hjelstuen, B.O., Eldholm, O., Faleide, J.I., 2007. Recurrent Pleistocene mega-failures on the SW Barents Sea margin. Earth Planet. Sci. Lett. 258 (3–4), 605–618. http://dx.doi.org/10.1016/j.epsl.2007.04.025.

Ilstad, T., Elverhøi, A., Issler, D., Marr, J.G., 2004. Subaqueous debris flow behaviour and its dependence on the sand/clay ratio: a laboratory study using particle tracking. Mar. Geol. 213 (1–4), 415–438. http://dx.doi.org/10.1016/j.margeo.2004.10.017.

Imbo, Y., De Batist, M., Canals, M., Prieto, M.J., Baraza, J., 2003. The Gebra Slide: a submarine slide on the Trinity Peninsula Margin, Antarctica. Mar. Geol. 193, 235–252. http://dx.doi.org/10.1016/S0025-3227(02)00664-3.

Jakobsson, M., Mayer, L., Coakley, B., Dowdeswell, J.A., Forbes, S., Fridman, B., Hodnesdal, H., Noormets, R., Pedersen, R., Rebesco, M., Schenke, H.W., Zarayskaya, Y., Accettella, D., Armstrong, A., Anderson, R.M., Bienhoff, P., Camerlenghi, A., Church, I., Edwards, M., Gardner, J.V., Hall, J.K., Hell, B., Hestvik, O., Kristoffersen, Y., Marcussen, C., Mohammad, R., Mosher, D., Nghiem, S.V., Pedrosa, M.T., Travaglini, P.G., Weatherall, P., 2012. The International Bathymetric Chart of the Arctic Ocean (IBCAO) version 3.0. Geophys. Res. Lett. 39 (12), L12609. http://dx.doi.org/10.1029/2012GL052219.

Jansen, E., Raymo, M.E., Blum, P., Shipboard Scientific Party, 1996. 9. Site 986. In: Proceedings of the Ocean Drilling Program, Initial Reports, 162, College Station, TX (Ocean Drilling Program), pp. 287–343. http://dx.doi.org/10.2973/odp.proc.ir.162.

109.1996.
Kandilarov, A., Landa, H., Mjelde, R., Pedersen, R.B., Okino, K., Murai, Y., 2010. Crustal structure of the ultra-slow spreading Knipovich Ridge, North Atlantic, along a presumed ridge segment center. Mar. Geophys. Res. 31 (3), 173–195. http://dx.doi.org/10.1007/s11001-010-9095-8.
Kim, D.C., Sung, J.Y., Park, S.C., Lee, G.H., Choi, J.H., Kim, G.Y., Seo, Y.K., Kim, J.C., 2001. Physical and acoustic properties of shelf sediments, the South Sea of Korea. Mar. Geol. 179 (1–2), 39–50. http://dx.doi.org/10.1016/S0025-3227(01)00200-6.
Laberg, J.S., Vorren, T.O., 1996a. The Middle and Late Pleistocene evolution of the Bear Island Trough Mouth Fan. Glob. Planet. Chang. 12 (1–4), 309–330. http://dx.doi.org/10.1016/0921-8181(95)00026-7.
Laberg, J.S., Vorren, T.O., 1996b. The glacier-fed fan at the mouth of Storfjorden trough, western Barents Sea: a comparative study. Int. J. Earth Sci. 85 (2), 338–349. http://dx.doi.org/10.1007/BF02422239.
Laberg, J.S., Vorren, T.O., Mienert, J., Bryn, P., Lien, R., 2002. The Trænadjupet Slide: a large slope failure affecting the continental margin of Norway 4000 years ago. Geo-Mar. Lett. 22 (1), 19–24. http://dx.doi.org/10.1007/s00367-002-0092-z.
Le Ravalec, M., Guéguen, Y., 1996. High- and low-frequency elastic moduli for a saturated porous/cracked rock-differential self-consistent and poroelastic theories. Geophysics 61 (4), 1080–1094. http://dx.doi.org/10.1190/1.1444029.
Llopart, J., Urgeles, R., Camerlenghi, A., Lucchi, R.G., De Mol, B., Rebesco, M., Pedrosa, M.T., 2014. Slope instability of glaciated continental margins: constraints from permeability-compressibility tests and hydrogeological modeling off Storfjorden, NW Barents Sea. In: Krastel, S., Behrmann, J.-H., Völker, D., Stipp, M., Berndt, C., Urgeles, R., Chaytor, J., Huhn, K., Strasser, M., Harbitz, C.B. (Eds.), Submarine Mass Movements and Their Consequences, Advances in Natural and Technological Hazards Research. 37. pp. 95–104. http://dx.doi.org/10.1007/978–3–319-00972-8-9.
Llopart, J., Urgeles, R., Camerlenghi, A., Lucchi, R.G., Rebesco, M., De Mol, B., 2015. Late Quaternary development of the Storfjorden and Kveithola Trough Mouth Fans, northwestern Barents Sea. Quat. Sci. Rev. 129, 68–84. http://dx.doi.org/10.1016/j.quascirev.2015.10.002.
Lucchi, R.G., Pedrosa, M.T., Camerlenghi, A., Urgeles, R., De Mol, B., Rebesco, M., 2012. Recent submarine landslides on the continental slope of Storfjorden and Kveithola Trough-Mouth Fans (North West Barents Sea). In: Yamada, Y., Kawamura, K., Ikehara, K., Ogawa, Y., Urgeles, R., Mosher, D., Chaytor, J., Strasser, M. (Eds.), Submarine Mass Movement and Their Consequences, Advances in Natural and Technological Hazards Research. 31. Springer, Dordrecht (The Netherlands), pp. 735–745. http://dx.doi.org/10.1007/978-94-007-2162-3_65.
Lucchi, R.G., Camerlenghi, A., Rebesco, M., Colmenero-Hidalgo, E., Sierro, F.J., Sagnotti, L., Urgeles, R., Melis, R., Morigi, C., Bárcena, M.-A., Giorgetti, G., Villa, G., Persico, D., Flores, J.-A., Rigual-Hernández, A.S., Pedrosa, M.T., Macri, P., Caburlotto, A., 2013. Postglacial sedimentary processes on the Storfjorden and Kveithola trough mouth fans: significance of extreme glacimarine sedimentation. Glob. Planet. Chang. 111, 309–326. http://dx.doi.org/10.1016/j.gloplacha.2013.10.008.
Madrussani, G., Rossi, G., Camerlenghi, A., 2010. Gas-hydrates, free-gas distribution and fault pattern on the west Svalbard continental margin. Geophys. J. Int. 180 (2), 666–684. http://dx.doi.org/10.1111/j.1365-246X.2009.04425.x.
Matheney, M.P., Nowack, R.L., 1995. Seismic attenuation values obtained from instantaneous-frequency matching and spectral ratios. Geophys. J. Int. 123, 1–15. http://dx.doi.org/10.1111/j.1365-246X.1995.tb06658.x.
Mosher, D.C., Shimeld, J., Hutchinson, D., Lebedeva-Ivanova, N., Chapman, C.B., 2012. Submarine landslides in Arctic sedimentation: Canada Basin. In: Yamada, Y., Kawamura, K., Ikehara, K., Ogawa, Y., Urgeles, R., Mosher, D., Chaytor, J., Strasser, M. (Eds.), Submarine Mass Movements and Their Consequences, Advances in Natural and Technological Hazards Research. 31. Springer, Dordrecht (The Netherlands), pp. 147–157. http://dx.doi.org/10.1007/978-94-007-2162-3-13.
Mosher, D.C., Campbell, D.C., Gardner, J.V., Piper, D.J.W., Chaytor, J.D., Rebesco, M., 2017. The role of deep-water sedimentary processes in shaping a continental margin: the Northwest Atlantic. Mar. Geol. http://dx.doi.org/10.1016/j.margeo.2017.08.018. (in press, Available online).
Nur, A., Mavko, G., Dvorkin, J., Gal, D., 1995. Critical porosity: the key to relating physical properties to porosity in rocks. In: Proc. 65th Annual International Meeting Society of Exploration Geophysicists Abstracts. 14 (1). pp. 878–881. http://dx.doi.org/10.1190/1.1887540.
Ó Cofaigh, C., Taylor, J., Dowdeswell, J.A., Pudsey, C.J., 2003. Palaeo-ice streams, trough mouth fans and high-latitude continental slope sedimentation. Boreas 32 (1), 37–55. http://dx.doi.org/10.1080/03009480310001858.
Ó Cofaigh, C., Dowdeswell, J.A., Kenyon, N.H., 2006. Geophysical investigations of a high-latitude submarine channel system and associated channel-mouth lobe in the Lofoten Basin, Polar North Atlantic. Mar. Geol. 226 (1–2), 41–50. http://dx.doi.org/10.1016/j.margeo.2005.09.014.
Ogata, K., Pogačnik, Ž., Pini, G.A., Tunis, G., Festa, A., Camerlenghi, A., Rebesco, M., 2014. The carbonate mass transport deposits of the Paleogene Friuli Basin (Italy/Slovenia): internal anatomy and inferred genetic processes. Mar. Geol. 356, 88–110. http://dx.doi.org/10.1016/j.margeo.2014.06.014.
Omosanya, K.O., Harishidayat, D., Marheni, L., Johansen, S.E., Felix, M., Abrahamson, P., 2016. Recurrent mass-vasting in the Sørvstnaget Basin Southwestern Barents Sea: a test of multiple hypotheses. Mar. Geol. 376, 175–193. http://dx.doi.org/10.1016/j.margeo.2016.03.003.
Pedrosa, M.T., Camerlenghi, A., De Mol, B., Urgeles, R., Rebesco, M., Lucchi, R.G., shipboard participants of the SVAIS and EGLACOM Cruises, 2011. Seabed morphology and shallow sedimentary structure of the Storfjorden and Kveithola trough-mouth fans (North West Barents Sea). Mar. Geol. 286 (1–4), 65–81. http://dx.doi.org/10.1016/j.margeo.2011.05.009.
Piper, D.J.W., Campbell, D.C., Mosher, D.C., 2016. Mid-latitude complex trough-mouth fans, Laurentian and Northeast fans, eastern Canada. Geol. Soc. Mem. 46 (1), 363–364. http://dx.doi.org/10.1144/M46.93.
Rajan, A., Mienert, J., Bünz, S., Chand, S., 2012. Potential serpentinization, degassing, and gas hydrate formation at a young (< 20 Ma) sedimented ocean crust of the Arctic Ocean ridge system. J. Geophys. Res. 117, B03102. http://dx.doi.org/10.1029/2011JB008537.
Rebesco, M., Camerlenghi, A., 2008. Late Pliocene margin development and mega debris flow deposits on the Antarctic continental margins: evidence of the onset of the modern Antarctic Ice Sheet? Palaeogeogr. Palaeoclimatol. Palaeoecol. 260, 149–167. http://dx.doi.org/10.1016/j.palaeo.2007.08.009.
Rebesco, M., Neagu, R.C., Cuppari, A., Muto, F., Accettella, D., Dominici, R., Cova, A., Romano, C., Caburlotto, A., 2009. Morphobathymetric analysis and evidence of submarine mass movements in the western Gulf of Taranto (Calabria margin, Ionian Sea). Int. J. Earth Sci. 98 (4), 791–805. http://dx.doi.org/10.1007/s00531-009-0429-1.
Rebesco, M., Liu, Y., Camerlenghi, A., Winsborrow, M., Laberg, J.S., Caburlotto, A., Diviacco, P., Accettella, D., Sauli, C., Tomini, I., Wardell, N., 2011. Deglaciation of the western margin of the Barents Sea Ice Sheet - a swath bathymetric and sub-bottom seismic study from the Kveitehola Trough. Mar. Geol. 279 (1–4), 141–147. http://dx.doi.org/10.1016/j.margeo.2010.10.018.
Rebesco, M., Pedrosa, M.T., Camerlenghi, A., Lucchi, R.G., Sauli, C., De Mol, B., Madrussani, G., Urgeles, R., Rossi, G., Böhm, G., 2012. One million years of climatic generated landslide events on the northwestern Barents Sea continental margin. In: Yamada, Y., Kawamura, K., Ikehara, K., Ogawa, Y., Urgeles, R., Mosher, D., Chaytor, J., Strasser, M. (Eds.), Submarine Mass Movements and Their Consequences. Advances in Natural and Technological Hazards Research. 31. Springer, Dordrecht (The Netherlands), pp. 747–756. http://dx.doi.org/10.1007/978-94-007-2162-3-66.
Rebesco, M., Laberg, J.S., Pedrosa, M.T., Camerlenghi, A., Lucchi, R.G., Zgur, F., Wardell, N., 2014. Onset and growth of Trough-Mouth Fans on the North-Western Barents Sea margin - implications for the evolution of the Barents Sea/Svalbard Ice Sheet. Quat. Sci. Rev. 92, 227–234. http://dx.doi.org/10.1016/j.quascirev.2013.08.015.
Rebesco, M., Özmaral, A., Urgeles, R., Accettella, D., Lucchi, R.G., Rüther, D., Winsborrow, M., Llopart, J., Caburlotto, A., Lantzsch, H., Hanebuth, T.J.J., 2016. Evolution of a high-latitude sediment drift inside a glacially-carved trough based on high-resolution seismic stratigraphy (Kveithola, NW Barents Sea). Quat. Sci. Rev. 147, 178–193. http://dx.doi.org/10.1016/j.quascirev.2016.02.007.
Rossi, G., Gei, D., Böhm, G., Carcione, J.M., Madrussani, G., 2007. Attenuation tomography: an application to gas-hydrate and free-gas detection. Geophys. Prospect. 55 (5), 655–669. http://dx.doi.org/10.1111/j.1365-2478.2007.00646.x.
Safronova, P.A., Andreassen, K., Laberg, J.S., Vorren, T.O., 2012. Development and post-depositional deformation of a Middle Eocene deep-water sandy depositional system in the Sørvestsaget Basin, SW Barents Sea. Mar. Pet. Geol. 36 (1), 83–99. http://dx.doi.org/10.1016/j.marpetgeo.2012.06.007.
Sallarès, V., Ranero, C.R., 2005. Structure and tectonics of the erosional convergent margin off Antofagasta, north Chile (23°30′S). J. Geophys. Res. 110, B06101. http://dx.doi.org/10.1029/2004JB003418.
Sauli, C., Rebesco, M., Camerlenghi, A., Urgeles, R., Diviacco, P., De Mol, B., Accettella, D., Liu, Y., Lucchi, R.G., 2010. Thin-skinned and giant submarine landslides on the southern Storfjorden Trough Mouth Fan (Barents Sea). In: Poster Presentation, EGU General Assembly, 2010, May 3–7 2010, Vienna (Austria). Geophysical Research Abstracts 12, EGU2010-15504.
Sawyer, D.E., Flemings, P.B., Dugan, B., Germaine, J.T., 2009. Retrogressive failures recorded in mass transport deposits in the Ursa Basin, Northern Gulf of Mexico. J. Geophys. Res. Solid Earth 114, B10102. http://dx.doi.org/10.1029/2008JB006159.
Schön, J.H., 1996. In: Helbig, K., Treitel, S. (Eds.), Physical Properties of Rocks: Fundamental and Principles of Petrophysics. (Seismic Exploration Series, No. 18). Pergamon Press, Tarrytown, New York, pp. 583.
Solheim, A., Berg, K., Forsberg, C.F., Bryn, P., 2005. The Storegga Slide complex: repetitive large scale sliding with similar cause and development. In: Marine and Petroleum Geology. Ormen Lange - An Integrated Study for the Safe Development of a Deep-water Gas Field Within the Storegga Slide Complex, NE Atlantic Continental Margin 22 (1–2). pp. 97–107. http://dx.doi.org/10.1016/j.marpetgeo.2004.10.013.
Stockwell Jr., J.W., 1997. Free software in education: A case study of CWP/SU: Seismic Un*x. Lead. Edge 16 (7), 1045–1050. http://dx.doi.org/10.1190/1.1437723.
Strasser, M., Henry, P., Kanamatsu, T., Thu, M.K., Moore, G.F., the IODP Expedition 333 Scientists, 2012. Scientific drilling of mass-transport deposits in the Nankai accretionary wedge: first results from IODP Expedition 333. In: Yamada, Y., Kawamura, K., Ikehara, K., Ogawa, Y., Urgeles, R., Mosher, D., Chaytor, J., Strasser, M. (Eds.), Submarine Mass Movements and Their Consequences, Advances in Natural and Technological Hazards Research. 31. Springer, Dordrecht (The Netherlands), pp. 671–681. http://dx.doi.org/10.1007/978-94-007-2162-3_60.
Sultan, N., Cochonat, P., Foucher, J.-P., Mienert, J., 2004. Effect of gas hydrates melting on seafloor slope instability. Mar. Geol. 213 (1–4), 379–401. http://dx.doi.org/10.1016/j.margeo.2004.10.015.
Talling, P.J., Wynn, R.B., Masson, D.G., Frenz, M., Cronin, B.T., Schiebel, R., Akhmetzhanov, A.M., Dallmeier-Tiessen, S., Benetti, S., Weaver, P.P.E., Georgiopoulou, A., Zuhlsdorff, C., Amy, L.A., 2007. Onset of submarine debris flow deposition far from original giant landslide. Nature 450, 541–544. http://dx.doi.org/10.1038/nature06313.
Taner, M.T., Koehler, F., Sheriff, R.E., 1979. Complex trace analysis. Geophysics 44 (6), 1041–1063. http://dx.doi.org/10.1190/1.1440994.
Taylor, J., Dowdeswell, J.A., Kenyon, N.H., 2000. Canyons and Late Quaternary sedimentation on the North Norwegian margin. Mar. Geol. 166 (1-4), 1–9. http://dx.doi.org/10.1016/S0025-3227(00)00010-4.
Taylor, J., Dowdeswell, J.A., Kenyon, N.H., Ó Cofaigh, C.S., 2002. Late Quaternary compositional architecture of trough-mouth fans: debris flows and suspended sediments on the Norwegian Sea margin. In: Dowdeswell, J.A., Ó Cofaigh, C.S. (Eds.),

Glacier-influenced Sedimentation on High-latitude Continental Margins. Geological Society, London, Special Publication 203. pp. 55–71. http://dx.doi.org/10.1144/GSL.SP.2002.203.01.04.

Urgeles, R., Leynaud, D., Lastras, G., Canals, M., Mienert, J., 2006. Back-analysis and failure mechanisms of a large submarine slide on the Ebro slope, NW Mediterranean. Mar. Geol. 226 (3–4), 185–206. http://dx.doi.org/10.1016/j.margeo.2005.10.004.

Vanneste, M., Guidard, S., Mienert, J., 2005. Bottom-simulating reflections and geothermal gradients across the western Svalbard margin. Terra Nova 17, 510–516. http://dx.doi.org/10.1111/j.1365-3121.2005.00643.x.

Vanneste, M., Mienert, J., Bünz, S., 2006. The Hinlopen Slide: a giant, submarine slope failure on the northern Svalbard margin. Arctic Ocean. Earth Planet. Sci. Lett. 245 (1–2), 373–388. http://dx.doi.org/10.1016/j.epsl.2006.02.045.

Volpi, V., Amblas, D., Camerlenghi, A., Canals, M., Rebesco, M., Urgeles, R., 2011. Late Neogene to Recent seafloor instability on the deep Pacific margin of the Antarctic Peninsula. In: Shipp, R.C., Weimer, P., Posamentier, H. (Eds.), Mass-transport Deposits in Deepwater Settings. SEPM Special Publication 96. pp. 161–177. http://dx.doi.org/10.2110/sepmsp.096.161.

Vorren, T.O., Laberg, J.S., 1997. Trough mouth fans - palaeoclimate and ice-sheet monitors. Quat. Sci. Rev. 16 (8), 865–881. http://dx.doi.org/10.1016/S0277-3791(97)00003-6.

Vorren, T.O., Laberg, J.S., Blaume, F., Dowdeswell, J.A., Kenyon, N.H., Mienert, J., Rumohr, J., Werner, F., 1998. The Norwegian-Greenland Sea continental margins: morphology and Late Quaternary sedimentary processes and environment. Quat. Sci. Rev. 17 (1-3), 273–302. http://dx.doi.org/10.1016./S0277-3791(97)00072-3.

Wang, Z., Wang, H., Cates, M.E., 2001. Effective elastic properties of solid clays. Geophysics 66 (2), 428–440. http://dx.doi.org/10.1190/1.1444934.

Westbrook, G.K., Chand, S., Rossi, G., Long, C., Bünz, S., Camerlenghi, A., Carcione, J.M., Dean, S., Foucher, J.-P., Flueh, E., Gei, D., Haacke, R.R., Madrussani, G., Mienert, J., Minshull, T.A., Nouzé, H., Peacock, S., Reston, T.J., Vanneste, M., Zillmer, M., 2008. Estimation of gas-hydrate concentration from multi-component seismic data at sites on the continental margins of NW Svalbard and the Storegga region of Norway. Mar. Pet. Geol. 25 (8), 744–758. http://dx.doi.org/10.1016/j.marpetgeo.2008.02.003.

White, J.E., 1975. Computed seismic speeds and attenuation in rocks with partial gas saturation. Geophysics 40 (2), 224–232. http://dx.doi.org/10.1190/1.1440520.

White, J.E., Mikhaylova, N.G., Lyakhovitskiy, F.M., 1975. Low-frequency seismic waves in fluid-saturated layered rocks. In: Izvestija Academy of Sciences USSR Physics of Solid Earth, Engl. Transl. 11. pp. 654–659.

Yamada, Y., Kawamura, K., Ikehara, K., Ogawa, Y., Urgeles, R., Mosher, D., Chaytor, J., Strasser, M., 2012. Submarine mass movements and their consequences. In: Yamada, Y., Kawamura, K., Ikehara, K., Ogawa, Y., Urgeles, R., Mosher, D., Chaytor, J., Strasser, M. (Eds.), Submarine Mass Movements and Their Consequences, Advances in Natural and Technological Hazards Research. 31. Springer, Dordrecht (The Netherlands), pp. 1–12. http://dx.doi.org/10.1007/978-94-007-2162-3.